Hunt for Majorana Quasiparticles

Master Thesis by

Saulius Vaitiekėnas

to

The Department of Physics
of the
Free University of Berlin

Supervised by

Prof. Dr. Piet Brouwer
and
Prof. Dr. Charles Marcus

Berlin, September 2016

There's no such thing as the unknown, only things temporarily hidden, temporarily not understood.

- Captain Kirk

Contents

Statutory Declaration

Hereby I confirm that I wrote this thesis independently and that I have not made use of any other resources or means than those indicated.

Saulius Vaitiekėnas

Acknowledgments

Listing everyone who contributed to this work would probably double the length of this document. Hence, as a symbol of my concerns about the rainforest, I would like to show my gratitude to everyone with a short but sincere 'Thank You' to all.

That being said I would like to exclusively thank three people without whom my work would not have been possible. I give my special thanks to Professor Charles Marcus for welcoming me into his experimental family and challenging me to expand my horizons. I express my appreciation to Professor Piet Brouwer for helping me to set and reach my goal. Last but not least, I thank Mingtang Deng for being friendly enough to tag me along on this extremely educational journey.

Abstract

Majorana excitations in certain condensed matter systems are predicted to exhibit exotic non-Abelian statistics. The elusive quasiparticles are their own quasiholes, thus possess zero energy. Consequently, a system suited for observing Majorana zero modes has two energetically degenerate ground states, reflecting the absence and presence of the quasiparticles. In theory, different ground states can be accessed by braiding the Majorana modes around each other. Such an experiment would resemble the main properties of the highly desired topological qubits.

Following theoretical blueprints, several experimental groups have undertaken the challenge to synthesize Majorana particles in the lab. Among numerous platforms that hypothetically host Majorana excitations, the biggest share of attention was received by one-dimensional topological superconductors posing Majorana zero modes at its ends. Albeit there are no known natural p-wave superconductors, they can be engineered by placing a material with strong spin-orbit coupling in a proximity to an ordinary s-wave superconductor and subjecting it to an external magnetic field. The former two features are intrinsically provided by epitaxial superconductor-semiconductor nanowires. Such nanowire equipped with a normal lead connected to one end and separated by a tunneling barrier from the rest of the system can be used as a tunneling spectrometer, therefore the density of states of the induced superconductor can be probed via low-temperature conductance measurements.

Spatial confinement has an interesting effect on the charge transport in one-dimensional nanowires. Due to the momentum quantization, charge carriers in semiconductor-superconductor hybrid nanowires form Andreev reflection mediated bound states. The corresponding modes are reflected in the proximitized semiconductor energy spectrum as discrete subgap states. Subject to an

external magnetic field the modes start to descend towards zero energy and become localized at the ends of the nanowire. Andreev bound states with the lowest energy eventually coalesce into a robust Majorana bound state with zero energy, signifying the topological phase transition.

This work introduces some Majorana-physics related theoretical background and discusses peculiarities of the Majorana quasiparticle hunting.

1

Introducing Topological Quantum Computation

The world's critical infrastructures being managed by the internet makes it difficult to imagine our modern society without computers. The rapid enhancing of technology requires to continue advancing from the fundamental point of view as well as to keep an eye open for possible alternatives. The following chapter provides a short introduction to the quantum computation and the role of topology in it.

1.1 From Classical to Quantum Computation

For more than half of the last century, the evolution of modern semiconductor industry has been following the well-known Moore's law [1]. Named after *Intel* co-founder Gordon E. Moore, the law predicts the exponential advance in semiconductor manufacturing. More precisely, it states that the number of transistors on a chip, that is electronic switches assembling logical circuits, should double every two years, decreasing in costs almost at the same rate.

It is startling that the modern technology has kept its pace with Moore's law for so long. Nevertheless, the size of transistors has a lower boundary, of which the order of magnitude is determined by Bohr radius, the characteristic size of atoms and molecules. Therefore, it does not come as a surprise that an exponential growth can not continue forever. Furthermore, the *Intel* architecture is developed for linear computing and even though it is still very relevant on a daily basis, real-time data processing is getting more intense and therefore more efficient performance of complex simulations is desired. These issues have motivated to look for alternative ways of computing.

Already in 1985, Richard P. Feynman theorized about the possibility of shrinking the bits to the size of atoms, thus introducing the computation to the quantum realm [2]. This idea has started forming the concept of quantum computing and a decade later requirements for its physical implementation [3] have been formulated by David P. DiVincenzo, see Fig. 1.1.

1.2 DiVincenzo Criteria

Firstly, a quantum system to be a quantum computer has to have at least two well-defined states, for example, the spin of an electron or the polarization of a photon. Due to the analogy to their classical counterparts, these fundamental building blocks are called quantum bits or qubits. Despite their similarity, a qubit can be in a superposition of its both states, a quantum mechanical property not exhibited by conventional bits. Secondly, it should be possible to initialize the system to its ground state by either literally or figuratively cooling it down. Next, by exploiting quantum phenomena, such as entanglement, one should be able to manipulate the qubits in a way that corresponds to a logical gate. In the end, the result has to be measured by mapping the system to one particular states. Most importantly, the whole cycle hast to be carried out before

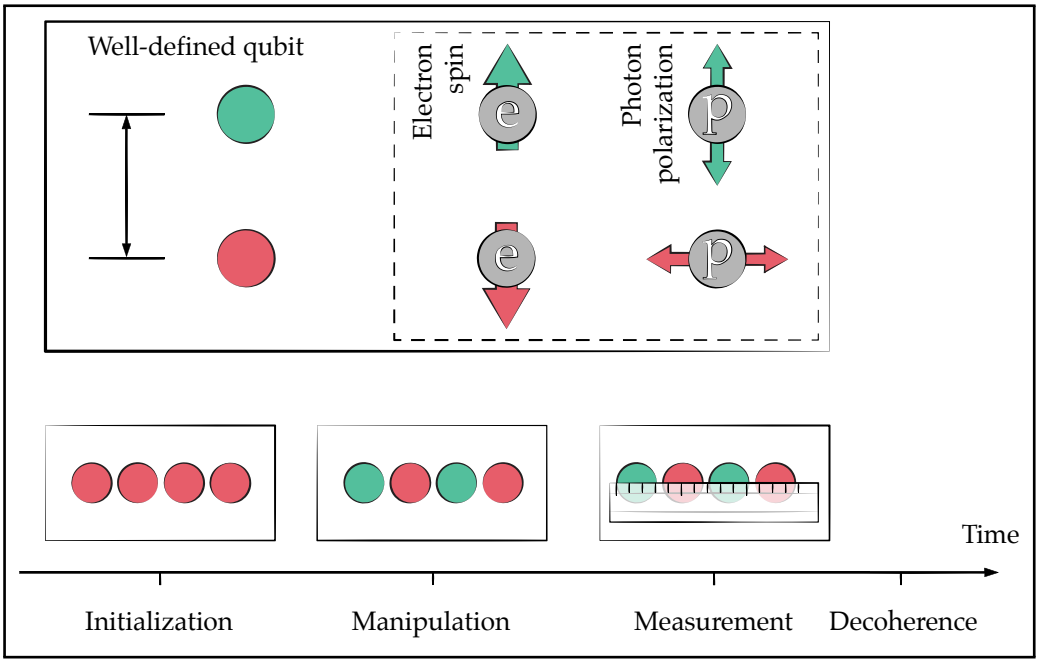

Figure 1.1: *Illustration of the five criteria for a quantum system to be used as a quantum computer. Proposed by David P. DiVincenzo [3].*

the wave function describing the quantum system loses the information it is carrying.

The last criterion is probably the most challenging to overcome experimentally. This is because realistic quantum systems are never truly isolated from their surroundings. After all, the only way of measuring it is by interaction. The loss of information contained in a quantum system due to the interaction with the environment is called decoherence, which is the source of the quantum errors and the biggest obstacle for realization of a quantum computer. While the classical computer errors are corrected by simply double checking the encoded information, the problem gets much more complex in quantum computers. In addition to the errors in form of a discrete qubit flip, which are similar to the digital ones, a quantum state may develop a continuous phase error, destroying the information contained in a superposition of the states. Intermediate state checking is not an option because it would lead to unavoidable wave collapse and loss of the information. It is possible to reduce the effects of decoherence for information stored in quantum memory by using a quantum analog of error correcting codes [4]. However, such algorithms by themselves require near error-free performance and are very difficult to implement. An alternative approach known as topological quantum computation addresses the matter differently from the fundamental point of view.

1.3 Topology

In mathematics, topology studies whether objects can be transformed continuously into each other. Knot theory is a close example to the topic of topological quantum computation. For instance, it is not hard to imagine that a circle, which is a trivial knot, can be transformed into an infinity shaped knot by simply twisting it around an arbitrary axis, see Fig. 1.2. This transformation is continuous and therefore these two knots are topologically equivalent. However, considering the simplest nontrivial knot, one realizes that there is no continuous way to transform it into a circle.

Analogously, in condensed matter physics, topology studies whether the Hamiltonians of two systems can be continuously transformed into each other. A quantum system with non-trivial topology would be insensitive to local perturbations and the information contained in this system's topological degrees of freedom would be automatically protected from decoherence [5].

Because of this extraordinary property, topological quantum computation has attracted a lot of attention, triggering the race in search of the first topological qubit. In order to clarify further analogy with the condensed matter physics

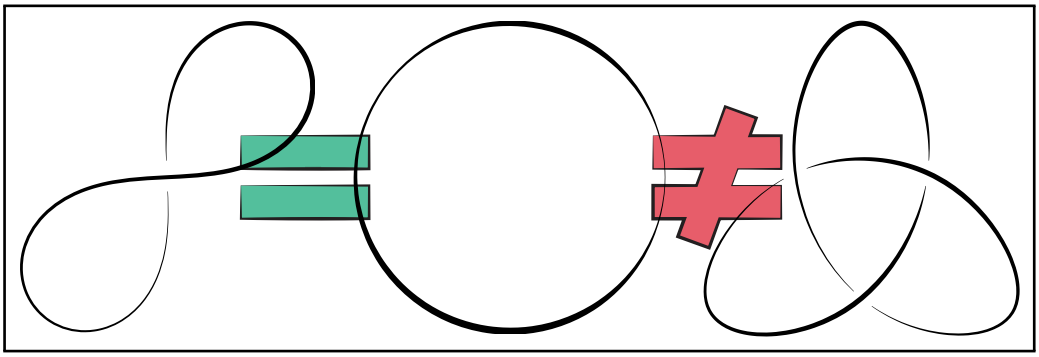

Figure 1.2: *In knot theory, a circle* ***(middle)****, which is a trivial knot, can be continuously transformed into a infinity shaped knot* ***(left)****. They are said to be topologically equivalent. The so-called trefoil knot* ***(right)*** *is the simplest nontrivial knot. There is no continuous way to transform it into a circle, hence it is topologically different from the other two.*

and demonstrate possible realization of the topological quantum qubit, it is helpful to get familiar with different types of particles.

1.4 Particle Exchange

Consider two fundamentally indistinguishable particles in three dimensions, described by the joint position quantum state $\psi(\mathbf{r}_1, \mathbf{r}_2)$. The exchange of two identical particles is a unitary transformation and can be represented by the exchange operator $\hat{P}$. Two consecutive exchanges - operation equivalent to one particle encircling the other - restores the two-particle wave function to its initial state $\hat{P}^2 |\psi(\mathbf{r}_1, \mathbf{r}_2)\rangle = |\psi(\mathbf{r}_1, \mathbf{r}_2)\rangle$. This indicates that the eigenvalues of $\hat{P}$ are $+1$ and -1, which essentially correspond to the classes of the particles. Particles described by a symmetric state are called bosons, whereas the ones described by an antisymmetric state are called fermions. The corresponding two particle wavefunctions evolve as

$$\hat{P} |\psi(\mathbf{r}_1, \mathbf{r}_2)\rangle = \quad |\psi(\mathbf{r}_2, \mathbf{r}_1)\rangle \quad \text{(bosons)}, \tag{1}$$

$$\hat{P} |\psi(\mathbf{r}_1, \mathbf{r}_2)\rangle = -|\psi(\mathbf{r}_2, \mathbf{r}_1)\rangle \quad \text{(fermions)}. \tag{2}$$

The fact that the motion of a particle being moved around the other does not get encoded in the two-particle wavefunction makes the whole concept of particle permutation in three dimensions rather mundane.

It gets more interesting if particles are confined in two dimensions, where the topology of the particle exchange starts to matter. Similarly to the previous example with the knot theory (see Fig. 1.2), the trajectories of the exchanged

particles cannot always be continuously transformed into different ones [5]. Because the space of particle trajectories is disconnected, the process of particles α and β being exchanged in a clockwise manner, see Fig. 1.3 left, is topologically different from the process of the same particles being exchanged in a counterclockwise manner, see Fig. 1.3 right.

Furthermore, even though the double counterclockwise exchange results in the initial particle configuration, due to the entangled trajectories the two-particle wavefunction adopts a phase factor $e^{i\phi}$, which depends only on the exchange topology and can be weighted freely with any ϕ between 0 and π. Consequently, these quasiparticles have been named anyons. The traces of two anyons moving around each other in time form braids, thus the motion is called braiding.

Anyons forming a system with a nondegenerate ground state obey Abelian statistics, *i.e.* braiding of such particles is commutative. Evolution of two Abelian anyon wavefunction due to counterclockwise exchange can be described as follows

$$\hat{P}\left|\psi\left(\mathbf{r}_1,\mathbf{r}_2\right)\right\rangle = e^{i\theta}\left|\psi\left(\mathbf{r}_2,\mathbf{r}_1\right)\right\rangle \quad \text{(Abelian anyons)}, \tag{3}$$

where the adopted phase $\theta = \phi/2$.

The Abelian anyons provide the basis for topologically fault-tolerant quantum memory in a form of product of phase factors gathered by a series of

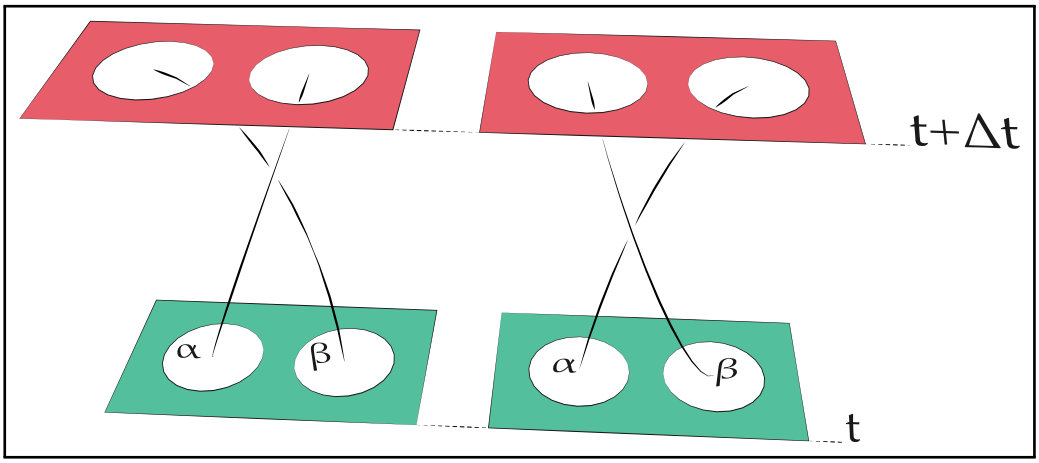

Figure 1.3: *In quantum mechanics there are only two distinguishable ways to exchange a pair of identical particles in two dimensions, namely counterclockwise* ***(left)*** *and clockwise* ***(right)****. Note that the third dimension represents time. Because the space of particle trajectories is disconnected, these two processes cannot be adiabatically deformed into each other.*

braidings. However, braiding of the Abelian anyons does not afford the implementation of arbitrary unitary transformation, hence there is no way to process the quantum information.

Non-Abelian anyons, on the other hand, form a system with a degenerate ground state. Braiding such quasiparticles brings the system from one ground state to another.

$$\hat{P}\left|\psi_a\left(\mathbf{r}_1,\mathbf{r}_2\right)\right\rangle = e^{i\theta U_{ab}}\left|\psi_b\left(\mathbf{r}_2,\mathbf{r}_1\right)\right\rangle \quad \text{(non-Abelian anyons)}, \tag{4}$$

where U_{ab} is a unitary matrix representing the transformation and is determined only by the topology of quasiparticle trajectory. Consecutive braidings result in a product of such unitary matrices, which in general do not commute. Therefore non-Abelian anyons intrinsically provide computational resource with purely topological nature [6].

The improvement of modern computers relies mainly on the geometric scaling of transistors. The downside of this approach is that the physical size limitation opposes the exponentially increasing density of electrical components. Therefore the enhancing of technology as it is known nowadays is slowing down and might eventually stop. These circumstances have motivated advancing beyond classical computation and so the criteria for quantum computation have been formulated. The essential requirements of a quantum computer is a two level system with accessible ground state, which can be manipulated and read out. The limiting time scale of a single process is intimately related to the coherence of the quantum state encoded in the qubit, which is very challenging to maintain due to arbitrary interactions with the environment. This problem could, in theory, be overcome by employing topological qubits, which are robust against local perturbations. Non-Abelian anyons are hypothetical quasiparticle excitations in condensed matter, following unique exchange statistics and therewith providing an excellent basis for the topological qubit. A candidate quasiparticle speculated to possess such properties is elaborated below.

2

Enter Majorana

In 1997 Alexei Kitaev theorized that due to their exotic exchange statistics non-Abelian anyons form a quantum system suitable to accommodate a topological qubit [7]. Majorana fermions as quasiparticle excitations are promising candidates for non-Abelian anyons. This chapter is concerned with an introduction to the rapidly growing field of topological quantum computation and Majorana physics [8].

2.1 From Fermions to Non-Abelian Anyons

One of the most common mechanisms believed to support non-Abelian anyons is quasiparticle excitation hosting Majorana zero mode. It is expected to occur in certain solid state systems and is the condensed matter analog of hypothetical elementary particle known as Majorana fermion (MF). The theoretical background of MF was formed by following the relativistic wave equation for electrons proposed by Paul Dirac in 1928 [9].

Combining quantum mechanics and special relativity, the British physicist discovered the theoretical framework for describing spin-½ particles. Dirac defined solutions suitable for his equation containing both real and imaginary numbers, indicating that the electron wavefunction has to be complex. This is consistent with the fact that electron is a particle with electrical charge and therefore can only be described with a complex wave function.

Interestingly, the complex conjugate of the wavefunction describing electron is also an eigenfunction of the Dirac's wave equation. The mathematical elegance leads to the prediction of electron's antiparticle, the positron, which was discovered in cosmic rays a few years later [10]. This supported Dirac's result forming the basic understanding of antimatter.

At that moment it seemed that the complex numbers are an unavoidable part of the solution to Dirac's equation. The picture, however, changed when in 1937 Italian physicist Ettore Majorana found solutions for the relativistic wave equation involving imaginary numbers only and still being consistent with quantum theory [11]. In this case, the modified Dirac's equation has physical meaning only if the wave function describing a spin-½ particle is real. Consequently, the corresponding particle has to be electrically neutral and its own antiparticle. Termed after their discoverer, a few elementary particles have been postulated to be Majorana fermions [12], however, none of them have been decisively confirmed in an experiment. In the very early 90s, it has been theorized that MFs can arise as zero energy quasiparticle excitations in certain solid state systems [13]. Due to their exotic fundamental properties, MFs in condensed matter have attracted immense attention.

2.2 Electrons in Condensed Matter

Condensed matter systems are usually described in terms of electrons forming a Fermi sea. An excitation of the system is called quasiparticle, which essentially corresponds to adding an excess electron to the system. A quasi-antiparticle is nucleated by removing an electron from the system and leaving a hole in its place. The hole behaves like a positively charged electron, hence considering it as a particle simplifies the description of electron interaction with a nearly full system.

In the second quantization language, the creation of an electron (annihilation of a hole) in a state i is described by a fermionic operator $c_i^\dagger$, whereas the annihilation process is described by its Hermitian conjugatec_i. The occupation of the state i can be determined with the corresponding number operator

$$n_i = c_i^\dagger c_i, \tag{5}$$

which has eigenvalues equal to 0 and 1, corresponding to empty and occupied states, respectively.

In general electrons follow Fermi-Dirac statistics characterized by three key relations between two arbitrary states associated with the quasiparticle and its hole [12]. First, due to the Pauli exclusion principle, the same state can be occupied by only one electron (or hole) indicating that

$$(c_i^\dagger)^2 = c_i^2 = 0. \tag{6}$$

Second, due to the antisymmetry of Fermi-Dirac statistics, two orthogonal states obey anticommutation relations

$$\{c_i, c_j\} = \{c_i^\dagger, c_j^\dagger\} = 0, \tag{7}$$

where the anitcommutator is defined by $\{a, b\} = ab + ba$. Third, the completeness relation gives

$$\{c_i, c_j^\dagger\} = \delta_{ij}. \tag{8}$$

Eqs. 6-8 are the evidence that electron can be distinguished form its hole and hence is not a Majorana fermion. On the other hand, there are known quasiparticle excitations in solid-state physics that are their own holes. As an example consider exciton, a bound state of an electron and a hole, which has a general form of

$$c_i^\dagger c_j + c_i c_j^\dagger. \tag{9}$$

It is transparent that complex conjugation yields the same expression, thus an exciton is its own antiparticle. Nevertheless, its spin is an integer number, hence effectively it is a boson. This prevents it from fitting into the framework of Majorana formalism.

It seems that MFs might be unfeasible by utilizing electrons in normal solid state systems, however, the picture changes in superconducting matter, where the boundary between particles and antiparticles is smeared out.

2.3 Superconductivity

An electron moving through a lattice generates a phonon, which in turn interacts with other electrons. This results in a finite attractive force between electrons. Normally, this force is negligible compared to the thermal excitations. At sufficiently low temperatures, however, in some materials the attractive force becomes comparable to other excitations and electrons start to form bound states called Cooper pairs.

A sudden loss of electrical resistance in certain materials below a characteristic critical temperature, that is the phenomenon of superconductivity, is mediated by the Cooper pairs [14]. Owing to their boson-like nature, bound pairs of electrons, condense into the same quantum ground state. Consequently, adding or removing a Cooper pair from the condensate does not change the overall state. This implies that the conservation of electron number is no longer valid. Furthermore, Cooper pairs are attracted by holes and repealed by electrons. This results in charge screening, that blurs out the particle-antiparticle

dichotomy. Moreover, an electron from a normal state lowers its energy by mixing with a hole and undergoing in the superconducting state. Such joint electron-hole excitation is termed Bogoliubov quasiparticle.

Most of the known superconductors exhibit s-wave pairing and Cooper pairs are formed of electrons with opposite spin projections [8]. The operator associated with the corresponding Bogoliubov quasiparticle can be expressed by

$$b = uc_{\uparrow}^{\dagger} + vc_{\downarrow}, \tag{10}$$

where the electron and hole components generically have different weights $(u \neq v)$. It seems that these quasiparticles are not the realization of MFs. Instead, Majorana modes are associated with a spinless operator with both of its components weighted equally. Such an operator can be constructed by approaching the issue from a different perspective.

2.4 Majorana Zero Modes

Every fermionic operator can be decomposed into its real and imaginary part, each of which is a MF, see the top panel of Fig. 2.1. This simply corresponds to a mathematical change of operator basis and firstly has no physical importance. That is because normally both components are tightly localized in space and their wave functions cannot be addressed individually, see left panel of Fig. 2.1. If, however, each part would happen to be spatially separated, they would yield a highly delocalized fermionic state, see right panel of Fig. 2.1, which would be immune to most types of decoherence, since no local perturbation could change it by affecting only one of the MFs.

In the second quantization language this can be expressed as

$$c_i = \frac{1}{2}\left(\gamma_{i,1} + i\gamma_{i,2}\right) \quad \text{and} \quad c_i^{\dagger} = \frac{1}{2}\left(\gamma_{i,1} - i\gamma_{i,2}\right). \tag{11}$$

The inverted relations read

$$\gamma_{i,1} = c_i^{\dagger} + c_i \quad \text{and} \quad \gamma_{i,2} = i(c_i^{\dagger} - c_i). \tag{12}$$

In contrast to the Bogoliubov quasiparticle operator given by Eq. 10, the new operators are Hermitian

$$\gamma_{i,\alpha}^{\dagger} = \gamma_{i,\alpha} \tag{13}$$

and hence Majorana operators. Furthermore, one can verify that

$$(\gamma_{i,1}^{\dagger})^2 = (\gamma_{i,2}^{\dagger})^2 = 1. \tag{14}$$

Any fermionic operator satisfying this condition can be associated with a propagating MF, of the type that neutrino is hypothesized to be, and can occur in superconductor of any type [15]. In other words, MF as the elementary particle is not related to the Hamiltonian of any system. However, an operator associated with a localized MF, also called Majorana zero mode (MZM), is system specific. That means that in addition to being fermionic and squaring to one, localized MZM commutes with the Hamiltonian of the system as

$$[\mathcal{H}, \gamma_{i,1}] = [\mathcal{H}, \gamma_{i,2}] = 0, \tag{15}$$

where the commutator is defined by $[a, b] = ab - ba$.

Eq. 14 has further implication on MZMs, namely adding a second quasiparticle to an already occupied state does not annihilate it, nor does it create a new state occupied by both quasiparticles. Instead, it recreates the state of zero occupancy [12]. Strictly speaking, the Pauli repulsion principle does not apply for MZMs and the attempt to count the occupation of Majorana mode comes to naught. Alternatively, the number states are provided through the normal fermion operator given by Eq. 5. In other words, a pair of MZMs can be either occupied or non-occupied with a single electron. The two degenerate states of a pair of MZMs correspond to the parity of superconductor, that is even or

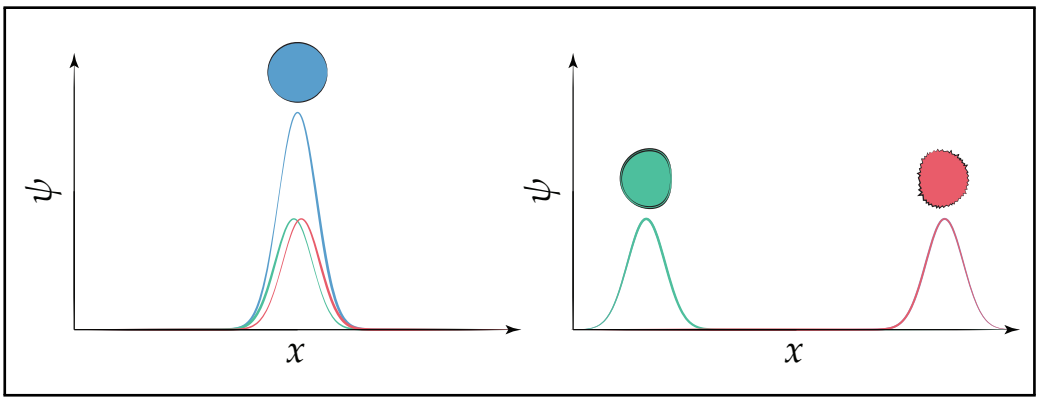

Figure 2.1: *Any fermionic operator (blue) can be decomposed into a real (green) and an imaginary (red) part, both of which are Majorana fermions. Spatially localized Majorana fermions merge to form a conventional fermion* ***(left)****, whereas spatially separated Majorana fermions yield a highly delocalized fermionic state* ***(right)****.*

oddness of the total electron number in the system. The ground state of a fixed parity system containing n Majorana mode pairs is 2^{n-1} fold degenerate.

Furthermore, it can be shown that MZM operators satisfy the anticommutation relation

$$\{\gamma_{i,\alpha}, \gamma_{j,\beta}\} = 2\delta_{ij}\delta_{\alpha\beta}, \tag{16}$$

which implies that Majorana modes, compared to the conventional fermionic particles (see Eqs. 7 and 8), follow different statistics. In particular, the process of exchanging two MZMs induces the transformation

$$\begin{aligned} \gamma_{i,\alpha} &\rightarrow \quad \gamma_{j,\beta}, \\ \gamma_{j,\beta} &\rightarrow -\gamma_{i,\alpha}. \end{aligned} \tag{17}$$

While the overall sign is a gauge choice, the additional minus sign signatures the braiding operation of non-Abelian anyons. Such an operation could in principle bring the system from one ground state to another. The ability to link the simple motions in physical space with the complex operations in exponentially large Hilbert space is what makes MZMs so attractive [16].

Localized MZMs are known to emerge at topological phase transitions or at topological defects in an ordered state [17]. The former scenario is predicted to occur in the fractional quantum Hall states with filling factor $\nu = 5/2$ [13], whereas the later can appear at vortices in a two-dimensional superconductor with $p_x \pm ip_y$ pairing [18] or at the domain walls of one-dimensional superconductor with p-wave pairing [19]. The advantage of the one-dimensional systems against the others lays in the relatively easy detection of MZMs, therefore it has the biggest focus of the current research. It can be described by an elegantly simple toy model.

2.5 1D Electron Chain

A Hamiltonian describing a one-dimensional system with spatially isolated MFs as eigenstates was first introduced by a Russian theoretical physicist Alexei Kitaev in 2001 [19]. It considers electrons as spinless fermions hopping along tight-binding chain consisting of N-sites with the p-wave superconducting pairing. In the second quantization language, it reads

$$\mathcal{H}_{chain} = \sum_{i}^{N} \left[-\mu c_i^\dagger c_i - t\left(c_i^\dagger c_{i+1} + c_{i+1}^\dagger c_i\right) + \Delta c_i c_{i+1} + \Delta^* c_i^\dagger c_{i+1}^\dagger \right]. \tag{18}$$

For simplicity, the chemical potential, μ, hopping amplitude, t, and supercon-

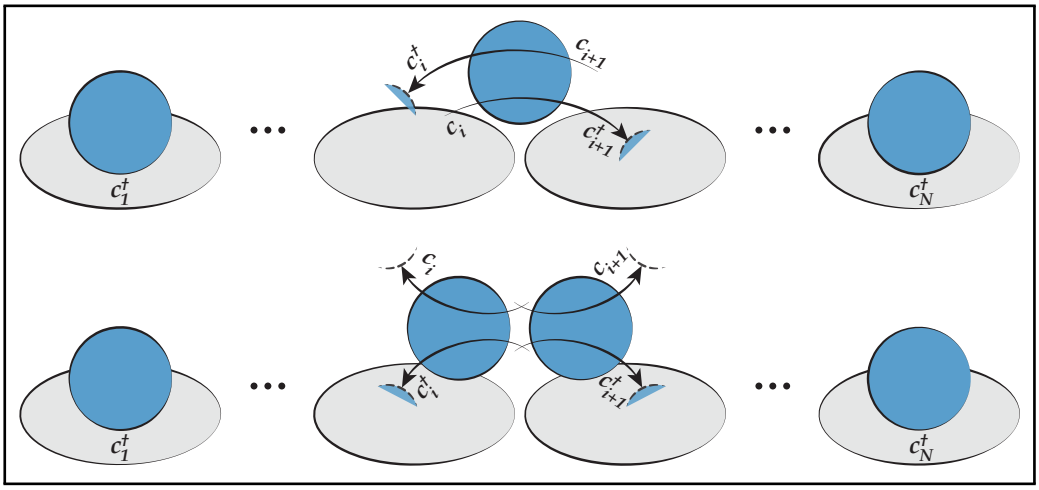

Figure 2.2: *Illustration of Hamiltonian describing 1D tight-binding chain with p-wave superconducting pairing, see Eq. 18. The tight binding term* ***(top)*** *allows electrons to hop between neighboring sites, whereas the superconducting terms* ***(bottom)*** *are responsible for Cooper pair creation and annihilation.*

ducting gap, $\Delta = |\Delta| e^{i\phi}$, are assumed to be constant for all sites. The first term of the Hamiltonian gives the energy contribution of an electron sitting on the i^{th} site. The hopping of electron between sites i and $i+1$ is illustrated in the top panel of Fig. 2.2. The bottom panel of Fig. 2.2 depicts the last two terms corresponding to the annihilation and creation of Cooper pairs, respectively. The superconducting term pairs electrons from neighboring sites with the same spin.

In order to make the Hamiltonian more transparent, it is convenient to absorb the superconducting phase, ϕ, into the definition of Majorana operators as

$$e^{i(\phi/2)} c_i = \frac{1}{2} \left(\gamma_{i,1} + i\gamma_{i,2} \right), \tag{19}$$

so the Eq. 18 can be rewritten in terms of Majorana operators

$$\mathcal{H}_{chain} = \frac{i}{2} \sum_{i}^{N} \left[-\mu \gamma_{i,1}\gamma_{i,2} + (t + |\Delta|)\, \gamma_{i,2}\gamma_{i+1,1} + (-t + |\Delta|)\, \gamma_{i,1}\gamma_{i+1,2} \right]. \tag{20}$$

In this form, the Hamiltonian reveals two distinct special cases. The first one corresponds to a trivial gapped phase and is centered around the point $\mu < 0$,

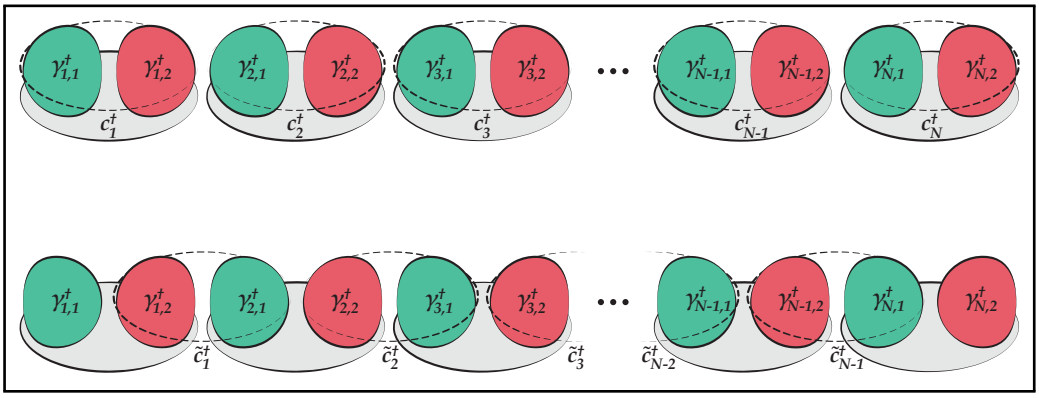

Figure 2.3: *Sketch of two limiting cases of Kitaev one-dimensional electron chain with tight binding and p-wave pairing. Fermionic operators $c_i^\dagger$ can be split into two Majorana operators $\gamma_{i,1}^\dagger$ and $\gamma_{i,2}^\dagger$. In the trivial case **(top)**, electrons are formed by Majorana operators from the same site. However, another limiting case **(bottom)** is possible where coupling between Majorana fermions from neighboring sites only is present. As a result, there are unpaired Majorana operators at the end of the wire.*

$t = |\Delta| = 0$. In this limit, the Hamiltonian simplifies to

$$\mathcal{H}'_{chain} = -\frac{i\mu}{2}\sum_i^N \gamma_{i,1}\gamma_{i,2} = -\mu\sum_i^N c_i^\dagger c_i, \tag{21}$$

and the ground state is formed by pairing Majorana operators from the same site, see the top panel of Fig. 2.3. There are no MZMs present in this limit. The more interesting case includes the points $\mu = 0$, $t = \pm|\Delta|$. Without loss of generality consider $t = |\Delta| > 0$, thus the Hamiltonian evolves to

$$\mathcal{H}''_{chain} = it\sum_i^N \gamma_{i,2}\gamma_{i+1,1} = 2t\sum_i^{N-1} \tilde{c}_i^\dagger \tilde{c}_i, \tag{22}$$

with the new fermionic operators defined as

$$\tilde{c}_i = \frac{1}{2}\left(\gamma_{i,2} + i\gamma_{i+1,1}\right) \quad \text{and} \quad \tilde{c}_i^\dagger = \frac{1}{2}\left(\gamma_{i,2} - i\gamma_{i+1,1}\right). \tag{23}$$

The latter limit also corresponds to a gapped phase, however, unlike in the trivial case, paired are the Majorana operators from neighboring sites, see the bottom panel of Fig. 2.3. Remarkably, there are unpaired Majorana operators at the ends of the chain, which do not appear in the Hamiltonian and hence

commute with it as

$$\{\gamma_{1,1}, \gamma_{N,2}\} = [\mathcal{H}, \gamma_{1,1}] = [\mathcal{H}, \gamma_{N,2}] = 0. \tag{24}$$

As a consequence, they are MZM operators. Furthermore, they can be combined into a single, non-local fermionic state

$$\tilde{c}_M = \frac{1}{2}\left(\gamma_{1,1} + i\gamma_{N,2}\right). \tag{25}$$

Most importantly, the occupation of this state requires zero energy. As a consequence there are two degenerate ground states which serve as topologically protected qubit states: $|0\rangle$ and $|1\rangle = \tilde{c}_M^\dagger |0\rangle$, where $\tilde{c}_M |0\rangle = 0$ [20].

Away from this limit, the Majorana end states appear in the Hamiltonian and thus no longer commute with it. However, it can be shown that generically MZMs persist under the condition that the chemical potential is maintained within the gap $|\mu| < 2t$. In this case, more complicated pair of operators are exponentially localized at the ends of the chain and satisfy

$$[\mathcal{H}, \gamma_{end}] \sim e^{-L/\xi}, \tag{26}$$

where L is the length of the chain and ξ is the superconducting coherence length [15]. As a consequence, the Majorana end states have finite energy, the splitting of which is exponentially suppressed with increasing wire length [21].

Realization of Kitaev's proposed chain experimentally requires a p-wave superconductor. There are speculations that A-phase of superfluid ^3He [22] and superconducting Sr_2RuO_4 [23] might possess some topological properties, however, these are not established materials yet and as of today there is no experimental evidence for natural superconductors with the p-wave pairing. Fortunately, this exotic paring can be engineered using readily available ingredients.

2.6 Majorana Zero Modes in Nanowires

In 2008, Liang Fu and Charles Kane [24] showed that coupling an ordinary s-wave superconductor to a strong topological insulator with surface states gives rise to proximity-induced [25], spinless $\mathrm{p}_x \pm i\mathrm{p}_y$-wave-like superconductivity in the topological insulator. Shortly after, several suggestions for simplifications followed and in 2010 two proposals by Roman Lutchyn *et al.* [26] and Yuval Oreg *et al.* [27], with recipes for synthesization of a one-dimensional topological

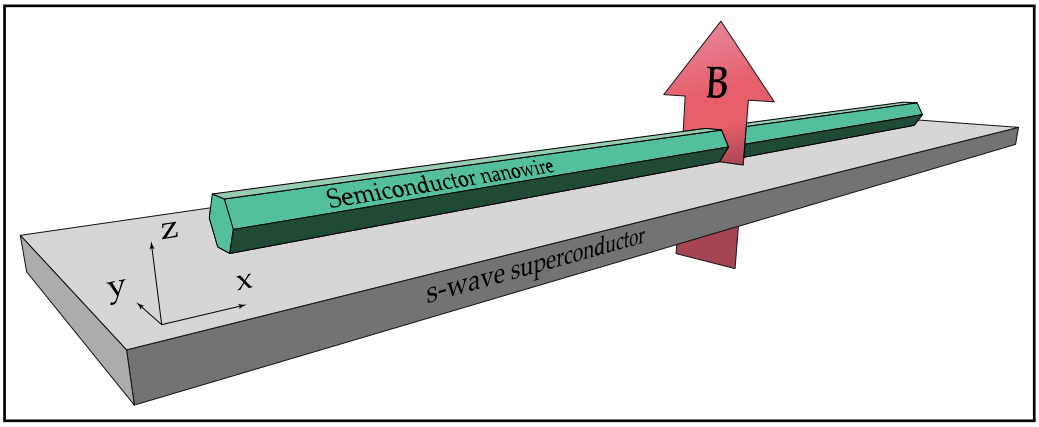

Figure 2.4: *Recipe for engineering topological superconductivity. A semiconductor nanowire is placed in proximity to an ordinary s-wave superconductor, which induces p-wave pairing in the wire. Placing the system into an external magnetic field nucleates Majorana fermions at the end of the nanowire.*

superconductor have been put forward. They both consider a semiconductor nanowire with strong spin-orbit interaction deposited on a conventional s-wave superconductor and placed in an external magnetic field, see Fig. 2.4.

The corresponding single particle Hamiltonian in the first quantization language is given by

$$\mathcal{H} = \left[\frac{k_x^2}{2m} - \mu\right]\tau_y + \alpha k_x \sigma_y \tau_y + E_z \sigma_z + \Delta\tau_z. \tag{27}$$

Without loss of generality, the wire is placed along the x-axis, Rashba spin-orbit interaction, α, acts along the y-axis and the external magnetic field with Zeeman energy, E_Z, is applied along the z-axis. The Pauli matrices σ_i and τ_i operate in spin space and couple particles and holes in real space, respectively.

The first term of Eq. 27 describes kinetic energy and the corresponding dispersion relation is a simple parabola, see the top left panel of Fig. 2.5. The offset in energy is given by the chemical potential, μ. For the moment consider $\mu = 0$.

Turning on the spin-orbit interaction shifts the two initially spin degenerate bands, depending on their spin polarization, along the momentum direction by $k_{so} = m\alpha$ and down in energy by $E_{so} = m\alpha^2/2$, see the top right panel of Fig. 2.5. The spin-orbit coupling does not break the time reversal symmetry, therefore spin degeneracy is still present for all energy values.

With superconductivity absent, to the spin-orbit field orthogonal external

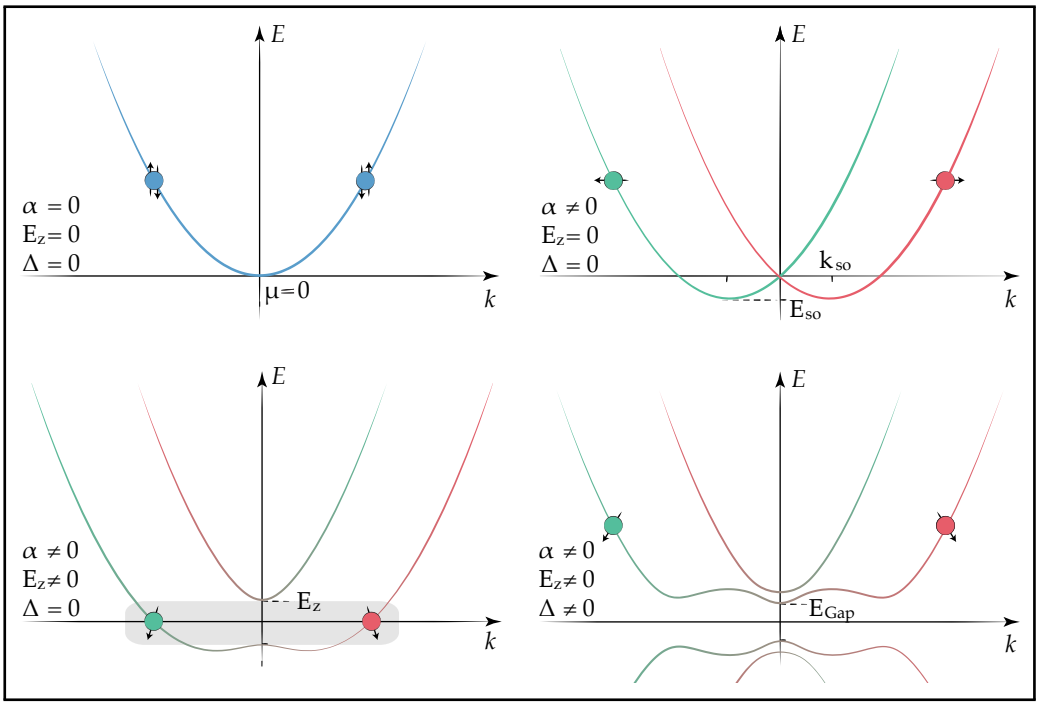

Figure 2.5: *Eigenvalue spectra of the Hamiltonian (see Eq. 27) describing a spin-orbit coupled semiconducting nanowire deposited on an ordinary s-wave superconductor placed in an external magnetic field. Each graph corresponds to the evolution of dispersion relation caused by consecutively turning on one term after another.* ***Top left:*** *The first term of the Hamiltonian describes the kinetic energy and the corresponding dispersion relation is a simple parabola offset in energy by mu.* ***Top right:*** *Turning on the spin-orbit interaction splits the spin-polarized bands. Note that the spin degeneracy is still present, since time-reversal symmetry is not broken.* ***Bottom left:*** *To the spin-orbint field orthogonal magnetic field turns the crossing at zero momentum into an anti-crossing. There is only one effective spin direction up to the Zeeman energy (indicated with a gray rectangle).* ***Bottom right:*** *Turning on the proximity-induced superconductivity opens up the topological gap between quasiparticle and hole band, which is necessary for the nucleation of Majorana zero modes.*

magnetic field, B_{ext}, breaks the time-reversal symmetry and turns the crossing at zero momentum into an anti-crossing, see the bottom left panel of Fig. 2.5. The size of the gap is given by the Zeeman energy $E_z = \frac{1}{2}0g\mu_B B_{ext}$, with semiconductor g-factor and Bohr magneton μ_B. There is only one effective spin direction in the range of $\pm E_z$. This gives rise to the so-called helical state. As a consequence, placing μ inside this range (the gray area in Fig. 2.5) allows inducing spinless superconductivity. It is worth mentioning that the spin direction inside the gap is still momentum dependent. As a matter of fact, the more spins are polarized the more difficult it is to induce the superconductivity since only antiparallel components of the spins will be coupled by the superconducting term.

The last term describes the proximity induced superconducting pairing. It results in a gapped dispersion relation, see the bottom right panel of Fig. 2.5. The quasiparticle and hole bands are separated by the superconducting gap, which is formed by the Cooper pair condensation around the Fermi energy. The minimum energy required to excite the superconducting state by breaking a Cooper pair is given by Δ. For small Δ, the effective superconducting gap is topological due to the external magnetic field and is associated with MZMs. Increasing Δ shrinks the gap, when at some point it closes completely, see the right panel of Fig. 2.6. For even larger values of Δ the gap opens again in a non-topological regime.

Phase transition between the trivial and topological superconducting states

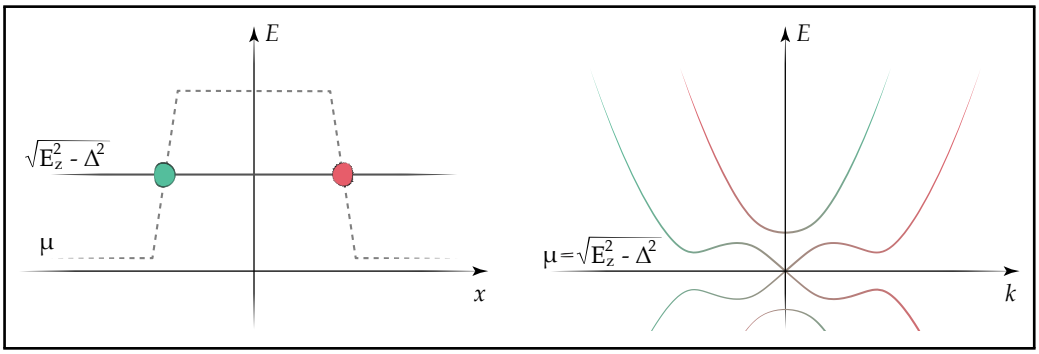

Figure 2.6: *Nucleation of Majorana zero modes.* ***Left:*** *The chemical potential of a wire can be tuned spatially with the help of capacitively coupled gate electrodes, allowing to enter the topological regime. MZMs (indicated in green and red) emerge whenever* μ *crosses* $\sqrt{E_z^2 - \Delta^2}$*, with* $E_Z > \Delta$*.* ***Right:*** *Dispersion relation at the phase transition* $\mu = \sqrt{E_z^2 - \Delta^2}$*. A single nondegenerate pair of states with equal spins and weights cross at Fermi energy, forming a MZM.*

occurs at the point where the gap closes. Continuously changing the parameters along the wire brings a single, nondegenerate pair of states with equal spins and weights to touch at Fermi energy and form a Majorana state. For the fixed value of the external magnetic field, the decisive point of the effective gap is at zero momentum. Its size extracted from Eq. 27 at $k_x = 0$, varies as

$$E_{Gap} = \left| E_Z - \sqrt{\Delta^2 + \mu^2} \right| . \tag{28}$$

In real systems, chemical potential can be tuned spatially by local gate electrodes capacitively coupled to the wire, allowing to define the position of topological phase transition. Eq. 28 indicates that for fixed magnetic field and superconducting gap, Majorana edge states will be nucleated whenever μ crosses $\sqrt{E_z^2 - \Delta^2}$, with the condition that $E_Z > \Delta$, see the left panel of Fig. 2.6.

2.7 Andreev Reflection

Properties of a material in a normal-conducting phase change radically when brought to the proximity of a material in a superconducting phase. Consider an electron propagating in a semiconductor at energy E and incident on the boundary of the superconductor. In the case of a perfect interface, the Fermi energies of both materials are aligned and for electrons with $E < \Delta$ there are no single quasiparticle states available in the superconductor. The only way for the electron to be scattered is by pairing with another electron at energy $-E$ from the Fermi sea of the semiconductor thereby forming a Cooper pair condensed at the Fermi surface in the superconductor. The condensation leaves a hole in the semiconductor Fermi sea. In order to satisfy the momentum conservation law, the hole is retroreflected in the reverse direction of the incident electron, while the Cooper pair continues propagating in the superconductor as supercurrent.

The charged transferred into the superconductor with a Cooper pair is $2e$, thus the conductance is doubled at the interface for electrons with energies smaller than the gap. This unique scattering was first explained in 1964 by a Russian theoretical physicist Alexander Andreev and hence is termed Andreev reflection [28]. The process is sketched in energy space in Fig. 2.7.

Electrons with $E \gtrsim \Delta$ start to scatter normally and thus only a portion of charge will be transmitted as supercurrent. For even higher energy electrons, supercurrent decays quickly and quasiparticle current arises.

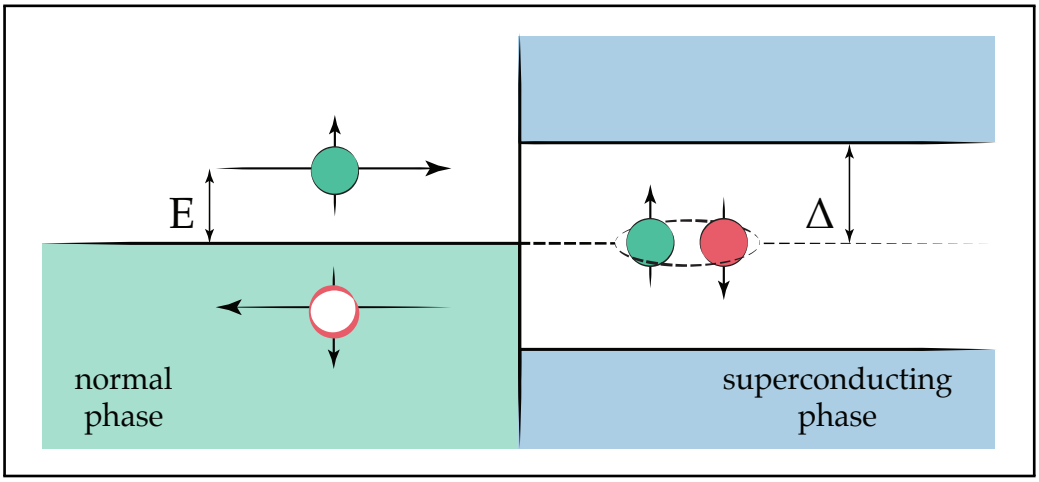

Figure 2.7: *Schematics of Andreev reflection at the boundary between normal and superconducting phases in energy space. From the normal phase point of view, an incident electron with energy $E < \Delta$ is retroreflected as a hole, whereas from the superconducting phase point of view, a Cooper pair is created at the interface.*

2.8 The BTK Model

The situation outlined above is idealized because the interface is assumed to be fully transparent. A more realistic scenario involves a potential barrier caused by impure boundary dividing the semiconductor and superconductor. This problem was first approached in 1982 by Greg Blonder, Michael Tinkham, and Teun Klapwijk [29]. A macroscopic derivation of this model was presented a few years later independently by Alexandre Zaitsev [30] and Gerald Arnold [31].

The original model considers a simple repulsive potential located at the interface. It can be advanced by regarding the mismatch of the semiconductor and superconductor Fermi energies, which can differ by a few orders of magnitude. This can lead to a potential step at the bottom of the conduction band at the interface. Nevertheless, for a qualitative picture, it is enough to consider δ-shaped potential

$$U(\mathbf{r}) = \frac{\hbar^2 k_F^S}{m_e} Z\delta(\mathbf{r}), \tag{29}$$

with k_F^S being the Fermi wave number in the superconductor. The height of the barrier is given by the dimensionless parameter Z.

An incoming electron from the semiconductor side is scattered in four different channels. It can be reflected as a hole or an electron with probabilities $A(E)$ and $B(E)$, respectively, or transmitted as a hole-like or an electron-like quasipar-

ticle with probabilities $C(E)$ and $D(E)$, respectively. Note that $A(E)$ describes the Andreev reflection and thus also contributes to transmission. The probabilities are determined by solving the Schrödinger equation for electrons and holes at the interface and are given in their full glory in Ref. [29]. Furthermore, the conservation of probability requires that $A(E) + B(E) + C(E) + D(E) = 1$. Utilizing Landauer formula [32] one gets transmission coefficient for electrical current, which is directly proportional to the differential conductance through the junction

$$\frac{dI}{dV} \propto 2A(E) + C(E) + D(E) = 1 + A(E) - B(E). \tag{30}$$

The effect of the superconducting gap on electrons with $E \to \infty$ is vanishing, in which case only the normal transmission is present. The differential conductance through the junction is hence obtained by normalizing Eq. 30 to the normal state conductance.

Fig. 2.8 depicts differential conductance through the boundary as a function of voltage applied between the semiconductor and superconductor for several barrier heights Z. As described above, with absent potential barrier, see the left panel of Fig. 2.8, electrons with energies below the gap are fully Andreev reflected. The conductance doubles at the interface due to the Cooper pair transmission into the superconductor. Outside the gap, the current carried by the Cooper pairs saturates rapidly and single quasiparticle current becomes evident. With a small potential barrier, see the middle panel of Fig. 2.8, the probability for electrons to be Andreev reflected is suppressed by the specular reflection. A peak caused by the retroreflection rises at the edge of the superconducting gap. In case of higher barriers, see the right panel of Fig. 2.8, specular reflection takes over within the gap, hence suppressing the conductance near to zero. All is left from the Andreev reflection is a narrow peak at $E = \Delta$.

In the tunneling barrier regime, that is for very high Z values, the transmission coefficient for electrical current given in Eq. 30 can be massaged into the form of BSC density of states $E/\sqrt{E^2 - \Delta^2}$ [33]. Furthermore, the bias voltage applied between the normal conductor and superconductor drops mostly at the interface. Therefore measuring differential conductance allows to directly probe the superconductor density of states. In case there is a Majorana zero mode located at the boundary, electrons with zero energy are Andreev reflected, resulting in zero bias peak in differential conductance measurements, with a theoretical height of $2e^2/h$, provided that the temperature is zero.

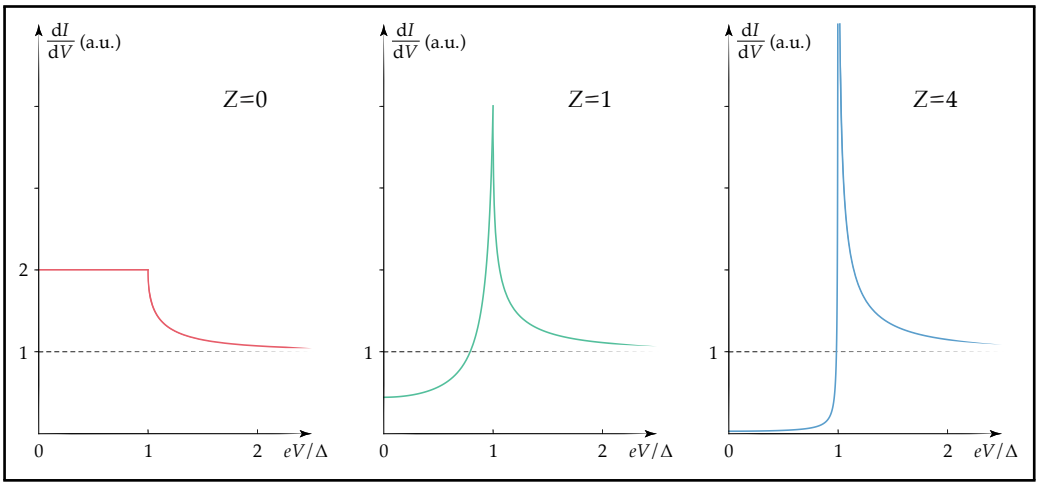

Figure 2.8: *Differential conductance as a function of voltage in units of superconducting gap for various barrier strengths Z at $T = 0$K. With the barrier absent **(left)**, Andreev reflection is the only process within the gap, whereas outside the gap it decays quickly and the specular reflection dominates. For increasing barrier **(middle)**, Andreev reflection peaks at the gap edge, but gets suppressed by the normal scattering within the gap. For very strong barriers **(right)**, the specular reflection dominates the transport and only a narrow band of electrons with $E \approx \Delta$ are Andreev reflected.*

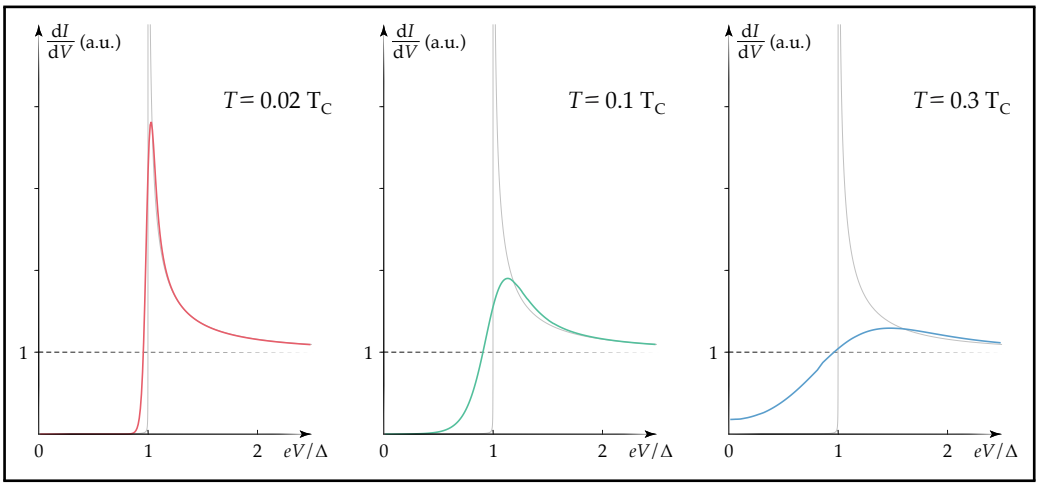

Figure 2.9: *Differential conductance as a function of voltage in units of superconducting gap for various temperatures T with the fixed barrier strength $Z \gg E/\sqrt{E^2 - \Delta^2}$. The gray curve in the background of each plot corresponds to the conductance at $T = 0$K. Already very small temperatures **(left)** smears the characteristic features and decreases the magnitude of the gap. Increasing the temperature **(middle)** shrinks the the gap further. Above a certain temperature **(middle)** only a slight decrease at $E < \Delta$ in differential conductance can be measured. The curve gets blurred toward a constant e^2/h value, corresponding to the normal phase conductance.*

In the discussion above the temperature was disregarded, however at any finite temperature the characteristic features get smeared out due to the thermal excitations. The temperature dependence of differential conductance is illustrated in Fig. 2.9, for $T = 0.02T_C$, $0.1T_C$ and $0.3T_C$, where T_C is the critical superconductor temperature above which the superconducting phase transits to the normal phase. As a reference, the curve in the limit of $Z \gg E/\sqrt{E^2 - \Delta^2}$ and $T = 0$ is plotted in the background of every plot. The effect is visible already for very small temperatures: the characteristic coherence peak at $E = \Delta$ decreases, while the quasiparticles start to leak into superconducting gap shrinking its magnitude. Higher temperature starts breaking up the Cooper pairs, gradually driving the superconductor normal. This increases the probability for electrons with $E \sim \Delta$ to tunnel as single quasiparticles. When the critical temperature is reached, the superconductivity is quenched resulting in quasiparticle tunneling for any value of E.

2.9 Proximity Effect

One of the assumptions made in BTK model is that the superconducting gap increases at the interface as a step function from 0 to a finite bulk value Δ. In this approach Andreev reflection gives rise to a nonzero pairing amplitude in the normal phase, however, the proximity induced superconductivity is absent [34]. This appears to be in contrast with the theoretical proposal introduced in Section 2.6, which relies on the gap in the semiconductor excitation spectrum opened by the Cooper pairs tunneling from the superconductor. These two seemingly divergent views of proximity effect are bridged in Ref. [35], where it is shown that the absence of the gap at the normal-conducting phase side of the boundary is an artifact of quasiclassical treatment of the problem.

The pioneering study on the proximity effect was carried out by French physicist Pierre-Gilles de Gennes in mid-1960s. The theoretical investigation showed that the properties of a superconductor get adopted by the normal conductor to a certain degree if these are coupled together. Furthermore, the results suggested that the proximity effect is mostly pronounced at the interface, whereas the normal phase is recovered within a characteristic length scale given by the material dependent coherence length. Unfortunately, the effect could not be investigated experimentally at the time due to the limited fabrication techniques. In 1996s, shortly after the patterning in submicron scales became available, several experiments reporting an induced gap in the normal conductor density of states were published [36,37]. The strong deviations from the BTK model suggested that there is an additional phenomenon allowing the

Cooper pair tunneling into the normal phase. In order to obtain a consistent interpretation of the measured results, the proximity effect had to be taken into account. This was firstly explained by generalizing the BTK model for the case of spatially inhomogeneous superconducting gap [38]. Some twenty years later the problem was treated quantum mechanically [35]. The outcome implied that the energy gap in the normal conductor is in general always present, whereas its magnitude depends on the parameters of both materials and the barrier height at the interface.

2.10 Experimental Study of MZMs

The first experimental signatures of a quasiparticle excitations matching the characteristics of the MZMs were observed in tunneling spectroscopy measurements [39, 40]. The general setup consisted of a semiconductor nanowire sourced with a superconductor proximitizing the wire at one end and drained with a normal metal or a superconductor at the other end. A tunneling barrier was then created in the uncovered segment of the wire between the leads by applying negative voltage to capacitively coupled gate electrodes, hence allowing to perform tunneling spectroscopy and probe the proximitized nanowire density of states. An emerging zero bias peak (ZBP) at finite magnetic field was observed and interpreted as Majorana excitation. Shortly after, several reports on signatures of MZMs in similar devices followed [41–45], backing up the first publications.

Note, however, that the quasiparticles are not explicitly claimed to be MZMs. That is because one can never rule out all the possible explanations of the ZBP. The incontestable hallmark of Majorana quasiparticles is the non-Abelian statistics, hence in the consecutive few years, a tremendous amount of effort has been put towards implementation of the braiding experiment [46].

First of all, the field took a huge step forward, when the nanowire heterostructures consisting of indium arsenide ($InAs$) and aluminum (Al) layers grown with epitaxially matched single-plane interfaces were developed [47]. The atomically clean interface has led to a number of fundamental improvements, in particular, hard induced superconducting gap with strongly reduced low energy excitations [48]. This has enabled quantitative study of near-zero-energy quasiparticle splitting. An exponential suppression of energy splitting consistent with the Majorana modes was observed as the modes become spatially separated [49]. Furthermore, double-quantum-dot devices made from the same nanowires have been studied and the ground state transitions between normal, superconducting and topological regimes have been shown [50].

Nevertheless, in spite of all the advances, the origin of MZMs has remained uncertain. The attempt of the current work is to clarify the origin and simplify the detection of MZMs.

Relativistic wave equation describing fermionic particles have two distinct complex solutions, which correspond to electron and its counterpart positron. Moreover, the equation can be modified so that its solutions are real, hence correspond to a fermionic particle, which is its own antiparticle. While the search of these hypothetical elementary particles called Majorana fermions continues, its analog as a quasiparticle excitation in certain condensed matter systems has been suggested. Majorana fermions in condensed matter, also known as Majorana zero modes, can be thought of as a real and imaginary part of an electron. If separated spatially, these two parts form a highly non-local and robust fermionic state. Controlled spatial manipulation of these modes would grant access to the non-Abelian statistics and thereby topological quantum computation. The simplest system with Majorana zero modes as eigenstates a tight-binding chain of electrons with the p-wave pairing. The system can be tuned into a regime with two energetically degenerate ground states. One of the states is filled with a Majorana zero mode, while the other is empty. This system is suitable to contain a topological qubit. In theory, it can be implemented in a semiconducting nanowire with a strong spin-orbit coupling, proximitized by an s-wave superconductor and subject to an external magnetic field. This combination induces a topologically non-trivial gap in the semiconductor and the Majorana zero modes are nucleated at points where the gap closes. The density of states of the proximitized nanowire, including the Majorana zero mode, can be probed by utilizing the tunneling spectroscopy. After the first experiments have identified signatures of Majorana modes in nanowires with proximity-induced superconductivity, an enormous progress in the field have been made, however, a better understanding of the MZM origin is still required. Some of the technical aspects used to fabricate and measure nanodevices designed to study Majorana modes are presented in the next chapter.

3

Submicron & Subkelvin

The following is a brief presentation of the fabrication process and measurement techniques of the devices reported in this thesis. The samples are prepared using electron beam lithography, whereas the measurements are carried out in a dilution refrigerator using standard lock-in techniques.

3.1 Lithography

Electron beam lithography (EBL) is a fundamental technique of nanofabrication allowing for patterning arbitrary submicron scaled features. In a sense, EBL is a scanning electron microscope (SEM) equipped with a pattern generator and beam blanker [51]. The lithography steps of the sample-patterning process are outlined schematically in Fig. 3.1.

The desired circuit is designed through a computer interface, whereas a base substrate is prepared by spin-coating it with a thin layer of polymeric material called resist. Usually, a positive resist is used, consisting of polymers (long chains of molecules), which are monomerized upon exposure to high-energy electrons. In order to get high-resolution features, electron scattering has to be considered. Electrons entering the resist start to break up the polymer chains, which slightly broadens the beam after every collision. The forward scattering can be reduced by increasing the incident electron energy and decreasing the thickness of the resist. High-energy electrons easily pass through the resist and penetrate deeply into the substrate, where they can reflect and reemerge at the surface, hence additionally exposing the resist. The backscattering can be compensated by software simulation, however, a small undercut is normally present.

After the exposure is done, the resist is developed in a solvent. The irradiated

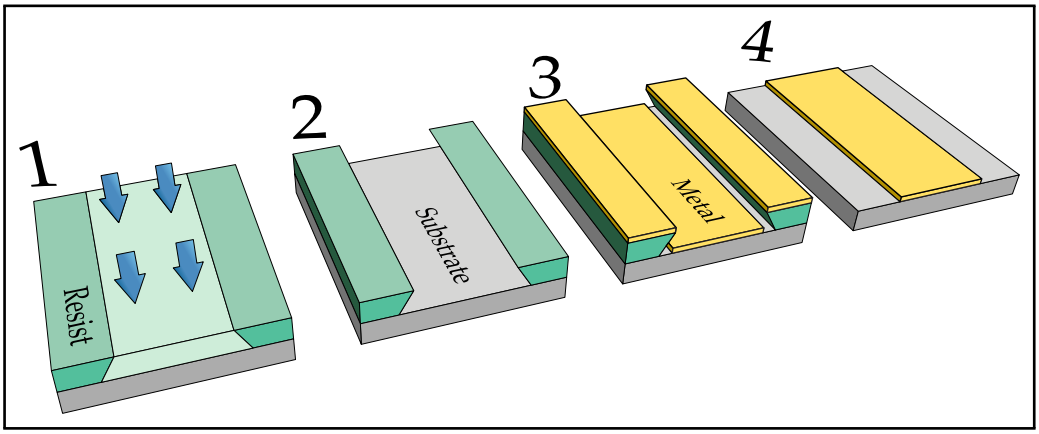

Figure 3.1: *Steps of electron beam lithography process.* ***1:*** *A substrate (gray) coated with a thin layer of resist (green) is irradiated by an electron beam (blue). A small undercut is present due to electron backscattering.* ***2:*** *The exposed chains of polymers are decomposed into a shorter molecules, allowing to selectively remove them via development in a solvent.* ***3:*** *The whole wafer is then covered with a thin film of metal or other material. The material directly sticks to the substrate at the previously exposed and developed parts, while the rest is protected by the resist.* ***4:*** *In the final step, the remaining resist is dissolved in a more aggressive solvent. In this way the unwanted material is removed, while the designed circuit is left intact.*

fragments of the polymer film are dissolved and removed, while the rest is left intact. The development is terminated by consecutive rinsing of the chip in a neutral solvent. Normally, this is a straightforward step, however, some care has to be taken to minimize the swelling as well as under- or over-development of the polymer. The performance can, in general, be improved by optimizing development duration and temperature according to exposure conditions, choice of resist and developer.

Once the wafer is cleaned, it is placed into a thin film deposition chamber. The whole surface of the wafer is covered by a layer of required metal or other material. Depending on the properties of the element or compound, it can be chosen to be deposited by the means of magnetron sputtering, electron beam evaporation or thermal evaporation. The material can directly stick to the previously exposed and developed areas of the substrate, whereas everywhere else the contact with the surface is prevented by the resist. During the procedure, a tilt and rotation can be applied to the sample, allowing to construct shadowed patterns, soft edges and more. For the next step it is important that the material at the exposed regions is well separated from the rest, thus big tilt angles and high layers, compared to the thickness of the resist, should be avoided.

Lastly, the remaining polymer film is removed together with the unwanted

metal. The wafer is immersed into a more aggressive solvent dissolving the resist and simultaneously lifting-off the material on top of it. However, the material sticking directly to the substrate is left intact, hence the desired pattern is obtained. The lift-off can be facilitated by exploiting bi-layer resist scheme. A broader undercut is formed by stacking resist with different sensitivities to the electron beam, while the resolution is preserved.

3.2 Recipe

All the devices discussed in this work are fabricated on a degenerately n-doped silicon (Si) substrate capped with a 200 nm silicon oxide (SiO_2) dielectric layer purchased from *Sil'tronix Silicon Technologies*. First of all, organic residues are cleaned off the Si wafer by using Piranha solution. The etching procedure is carried out in following order:

- Firstly, 45 mL of sulfuric acid (H_2SO_4) is poured into an empty thoroughly cleaned flat glass beaker.
- Secondly, 15 mL of hydrogen peroxide (H_2O_2) is added successively.
  Side note: Mixing these two chemicals together yields highly exothermic reaction. Wait 5 min before proceeding.
- The Si wafer is submerged into the solution for 10 min.
- The substrate is consecutively cleaned in at least two beakers of *Milli-Q* water and blown dry with nitrogen (N_2).
- Finally, the wafer is baked at 185 °C on a heating stage for 4 min.

At this point, the substrate is ready for lithography. There are several standard steps that are carried out in the same manner unless otherwise mentioned.

- Resist is spun at 4000 rpm for 45 s and successively baked at 115 °C for 120 s.
- Electron beam resist is developed in methyl isobutyl ketone (MIBK) 1:3 IPA solvent for 90 sec at room temperature. The development is terminated by rinsing the chip in IPA for 30 sec. The chip is then blown dry. Finally, the resist residuals are removed by ashing the chip with oxygen plasma for 60 sec.
- The lift-off is started by putting the chip into the acetone pre-warmed to 55 °C. After some 30 min to 60 min, the lift-off is finished by squeezing the warm acetone to the surface of the chip with a pipette, thus removing the unwanted metal. The chip is then rinsed in isopropanol (IPA) and blown dry with N_2.

For the sake of efficiency, the whole wafer is prepared with pre-fabricated blank chips in one go. The design of a blank chip, inspired by the previous students, is depicted in Fig. 3.2. One chip is divided into four quarters, so a higher number of devices can be fabricated at once. Each quarter is surrounded by 40 bonding pads, for the later device probing and contacting. Every bonding pad has a thin meander leading to the center of the chip, speeding up the later device exposures. For the precise exposures and on-chip orientation, a pattern of unique alignment marks is printed in the center and corners of each quarter of the chip.

The fabrication of blank chips is a two-step procedure in which the bonding pads and meanders are defined by means of photolithography using *Heidelberg µPG 501* LED writer, whereas alignment marks require higher resolution and hence are prepared by means of EBL using *Elionix ELS-7000* EBL system. The metallization is carried out utilizing *AJA* thin film deposition system. Generally, gold (*Au*) is the metal of choice with a thin sticking layer of titanium (*Ti*) underneath it. First, the bonding pads and meanders are fabricated as follows,

- AZ1505 photoresist is spun and baked for 120 s.
- Roughly 1 cm from the flat of the wafer is cleaved off using a ruler and a pen-scriber. This helps the LED writer to find the center of the chip.
- The bonding pads are exposed using 26 ms time constant & −6 defocus.

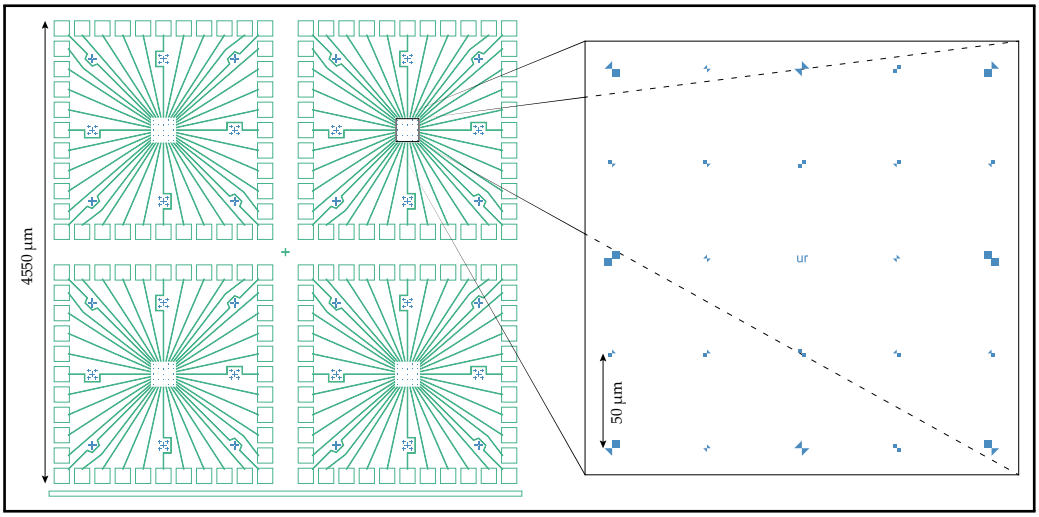

Figure 3.2: *Design of a blank chip.* ***Left:*** *Each chip is divided in four quarters. Bonding pads and meanders for the device contacting are indicated in green. Alignment marks for the on-chip orientation are indicated in blue.* ***Right:*** *Close-up of the upper-right quarter center. That is where the wires are deposited.*

- The wafer is developed in AZ400K solvent for 60 s and rinsed in *Milli-Q* water for another 60 s. The cleaning is finalized by blowing it dry and ashing.
- The metal evaporation is carried out in following order:
  - 5 nm of *Ti* with 10° tilt and 45 rpm rotation;
  - 25 nm of *Au* with 10° tilt and 45 rpm rotation;
  - 75 nm of *Au* with 0° tilt and 45 rpm rotation;
- The step is completed by the lift-off.

In order to reduce the systematic error from the stage drift while exposing the alignment marks, a bi-layer of sensitive resists is used, so a lower dose is required.

- First, a layer of MMA EL9 electron beam resist is spun and baked.
- Then, CSAR 4 % (AR-P 6200-04) electron beam resist is spun and baked.
- The alignment marks are exposed with 60 000 px per 600 µm resolution, 400 $\frac{\mu C}{cm^2}$ dose & 5 nA beam current.
- The development is started by putting the chip in o-Xylene solvent for 60 s, then continued by moving it to MIBK 1:3 IPA for another 30 s. It is terminated in IPA, thereafter the chip is blown dry and ashed.
- 5 nm of *Ti* and 80 nm of *Au* are evaporated with 0° tilt and 45 rpm rotation.
- After the lift-off a protective layer of 950kPMMA A6 resist is spun.
- The substrate is divided into separate chips with a diamond scriber.
- The protective layer is removed from each chip individually before using by dunking it in acetone for 5 minutes and rinsing it in IPA after.

Going through the steps listed above, one ends up with a batch of blank chips, ready for the device fabrication. The devices are composed of hexagonal *InAs*-core nanowires grown by molecular beam epitaxy (MBE) to a length of 5 µm to 10 µm, followed by low-temperature three-facet (half shell) epitaxial growth of *Al*. For more details about the material growth see Ref. [47].

The wires are deposited on the chip directly from the growth substrate with a help of a standard micromanipulator, see Fig. 3.3.1. After the deposition, the precise location of the wires (indicated in green in Fig. 3.3.2) is determined by imaging the chip with *Raith e-LiNE* SEM. Using *DesignCAD* software, the images are then imported into the chip design file, where the desired device circuit is prepared for the exposure.

The *Al* shell covers the wires throughout the whole length. As a consequence, applied gate voltage is screened by the metal. In order to create tunneling

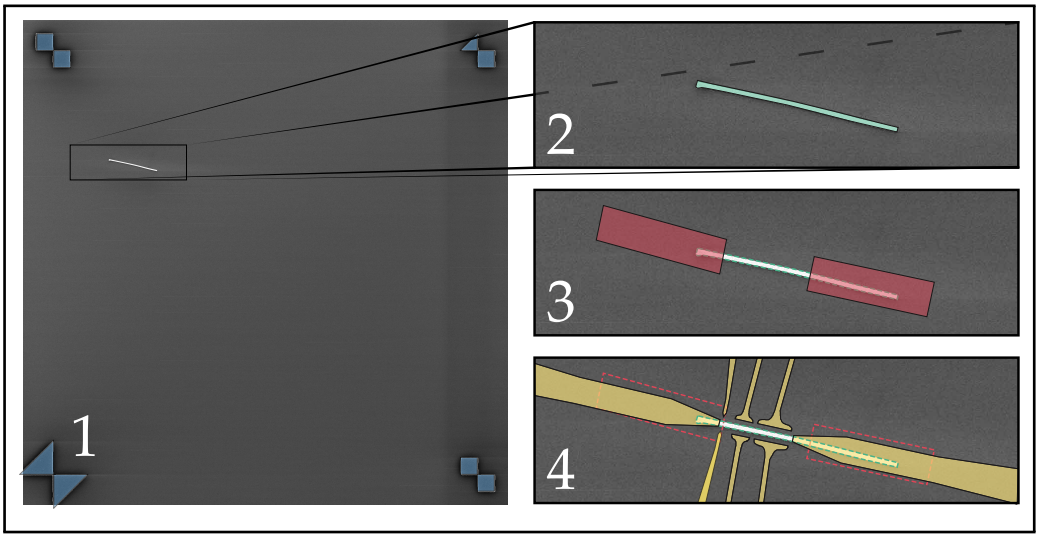

Figure 3.3: *Illustration of device fabrication.* ***1:*** *The wire are deposited on the chip using micromanipulator.* ***2:*** *The precise position of the wires is determined using scanning electron microscope.* ***3:*** *The Al shell is selectively removed from the wire in order to be able to create tunneling barriers.* ***4.*** *Gold contacts and gate electrodes are metalized in the last step.*

barriers, etching windows (indicated in red in Fig. 3.3.3) are opened in the resist and segments of *Al* are selectively removed using *Aluminum Etchant Type D* chemical etchant manufactured by *Transene Company Inc.*

- First, 950kPMMA A4 electron beam resist is spun and baked.
- The etching windows are exposed with 240 000 px per 600 µm resolution, 1000 $\frac{\mu C}{cm^2}$ dose & 440 pA beam current. Note that fine features such as etching windows require a higher dose.
- The chip is then developed and cleaned with plasma.
- In order to prevent the overrun of the etchant underneath the resist, the chip is post-baked at 115 °C for 60 sec.
- Two beakers, one with the *Al*-etchant another with the *Milli-Q* water, are pre-warmed to 55 °C. The chip is dipped into the etchant for 9 sec. Etching is terminated in the warm *Milli-Q* water.
- Finally, the chip is cleaned in another beaker with *Milli-Q* water for 60 sec, then blown dry and again cleaned with oxygen plasma.

To prevent the wires from moving or falling off completely, the fabrication is continued without removing the first layer of resist. Next, the contacts and gate electrodes (indicated in yellow in Fig. 3.3.4) are printed simultaneously in the final step.

- 950kPMMA A4 resist is spun on top of the first layer.

- The contact and gate pattern is exposed with 240 000 px per 600 µm resolution, 1100 $\frac{\mu C}{cm^2}$ dose & 440 pA beam current. A slightly higher dose is used because of the resist stacking.
- After the development the native layer of oxide is removed in AJA system. The chip is milled with 25 W argon (Ar) plasma for 8 min. The process is split into two 4 min steps with 5 min waiting in-between to avoid sample heating.
- The chip is metalized with
  - 5 nm of Ti with 10° tilt and 45 rpm rotation;
  - 25 nm of Au with 10° tilt and 45 rpm rotation;
  - 100 nm of Au with 0° tilt and 45 rpm rotation;
- After the lift-off the chip is again cleaned with oxygen plasma to remove any unwanted organic residuals.

Once the fabrication is complete, the devices are characterized at room temperature by measuring their resistance with *Lakeshore TTPX Cryogenic Probe Station*. The best looking devices are then bonded and prepared for the cool down.

3.3 Fridge

As mentioned above, see for example Fig. 2.9, investigation of quantum phenomena requires low temperatures, so the $k_B T$ does not overwhelm other relevant energy scales. For this reason, the measurements are performed in *Triton Cryofree* dilution refrigerator, also referred to as cryostat, with the base temperature, that is the lowest achievable temperature, of around 10 mK. The full cool-down of the system from room temperature to the base temperature is realized in two steps [52, 53].

In the first step, a gaseous mixture of two helium isotopes, $^3He - ^4He$, is circulated through the pre-cool loop, see Fig. 3.4. The cooling circuit is thermally coupled to a separate ^4He bath cooled to roughly 4 K using a pulse tube cooler. The pre-cool loop, therefore, cools the system by transferring the heat from the system to the pulse tube refrigerator. The process is continued until the temperature of mixing chamber, that is where the sample is mounted, is lowered to around 10 K. The mixture is then evacuated from the pre-cool loop using a turbo pump.

In the second step, the $^3He - ^4He$ mixture is condensed in the mixing chamber. For that, the gas is first pressurized with a compressor and refrigerated to roughly 4 K with the pulse tube cooler. It is then sent through a flow

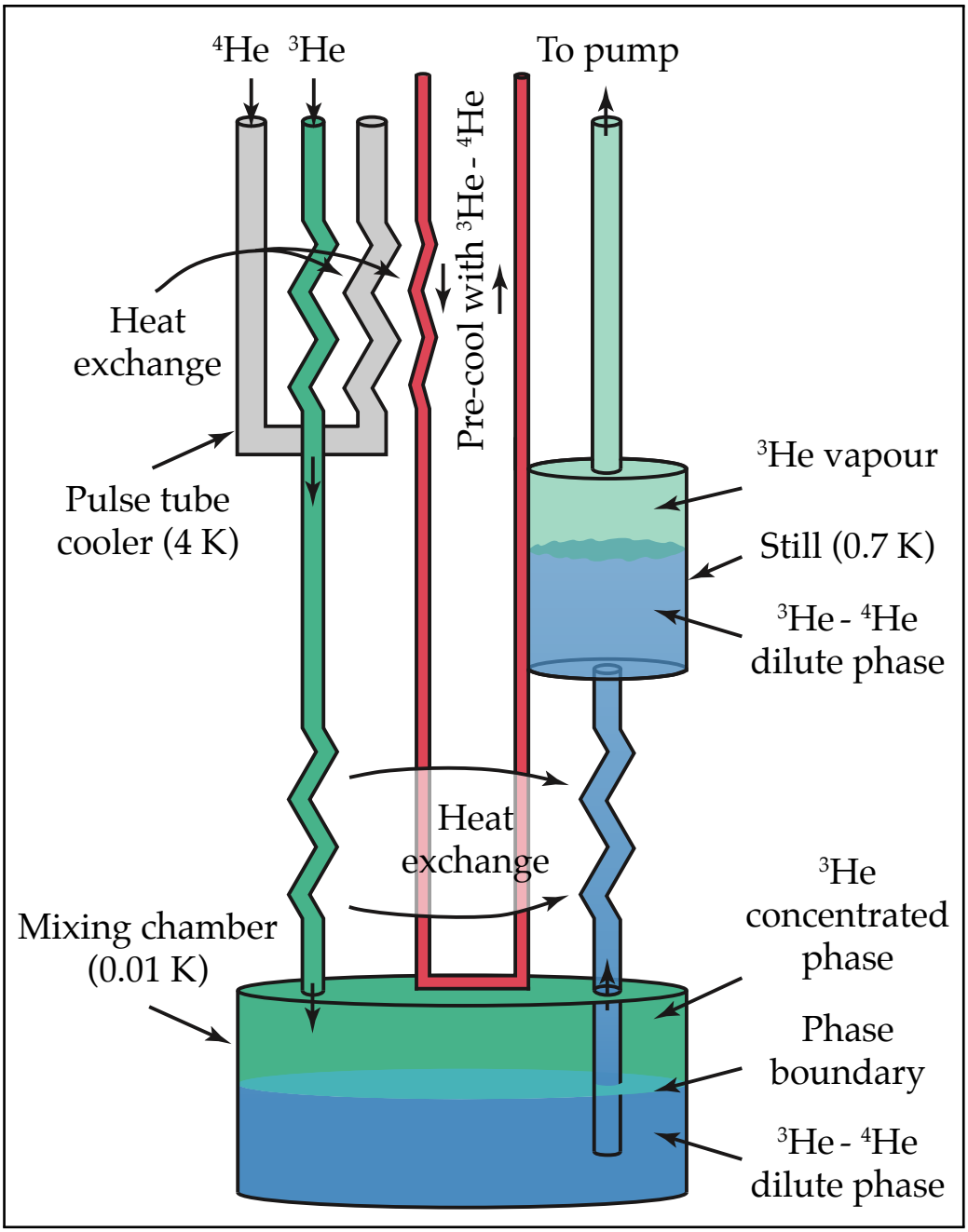

Figure 3.4: *Schematic of $^3He-^4He$ dilution refrigerator. In the first step of the cool down, the system is pre-cooled to around 10 K by circulating the $^3He-^4He$ mixture through a loop (red), which is cooled with a pulse tube cooler (gray) via thermal coupling. In the second step the mixture is condensed and sent to the mixing chamber. Liquid ^3He and ^4He mixing requires energy from surroundings, hence the chamber is cooled. The diluted mixture (blue) then flows to still, where ^3He is vaporized and looped back into the system with a pump.*

impedance, which further compresses, cools and eventually condenses the gas. The now liquid mixture flows through a series of heat exchangers and enters the mixing chamber, which ultimately reaches 0.01 K. The upper layer of liquid in the mixing chamber is highly concentrated ^3He, whereas the bottom layer is diluted mixture predominantly consisting of ^4He with a small fraction of ^3He. Due to the enthalpy difference between the concentrated and diluted phases, dilution cooling occurs at the phase boundary [54]. The diluted ^3He then flows to the still at roughly 0.7 K, where it is preferentially evaporated due to the lower boiling temperature. Finally, the again gaseous ^3He is recycled to a system by a pump continuing the cooling and maintaining the temperature of the mixing chamber at the base.

3.4 Setup

The measurements are performed exploiting standard alternating current (AC) lock-in techniques in 2-terminal setup illustrated in Fig. 3.5. An AC voltage signal sourced from *Stanford Research SR830* lock-in amplifier is applied to one of the sample leads termed source. This generates an AC current through the device, the signal of which is enhanced with a *Ithaco* current preamplifier connected to the other lead of the sample, referred to as drain, and measured with the same lock-in. The differential conductance of the device is obtained by digitally dividing the measured current with the applied voltage.

Both the strength and the broadening of the signal increase as a function of the applied voltage, hence a compromise between these two has to be found. One of the most relevant energy scales is the size of the superconducting gap, which normally is a few hundreds of µeV. Therefore, an excitation signal of a few µeV seems like a reasonable choice. In order to increase the resolution of the signal, voltage with higher amplitude is sourced first and then divided by a factor of around 1 : 17700 using a home built voltage divider before applying it to the sample.

Such a measurement provides information about the sample spectrum only around zero energy. The broader spectrum is obtained by superimposing the sinusoidal signal on a direct current (DC) voltage signal sourced from a custom built digital-to-analog converter (DAC). Foremost, the DC signal is enhanced by a factor of roughly 1 : 350 using the same home built voltage divider. Thereafter it is combined with the enhanced AC signal. The signal-to-noise ratio of the superimposed signal is further increased by a series of RC and radio frequency filters. The filters are also meant to reduce the effective electron temperature, which is mostly the biggest source of thermal broadening. Performing the

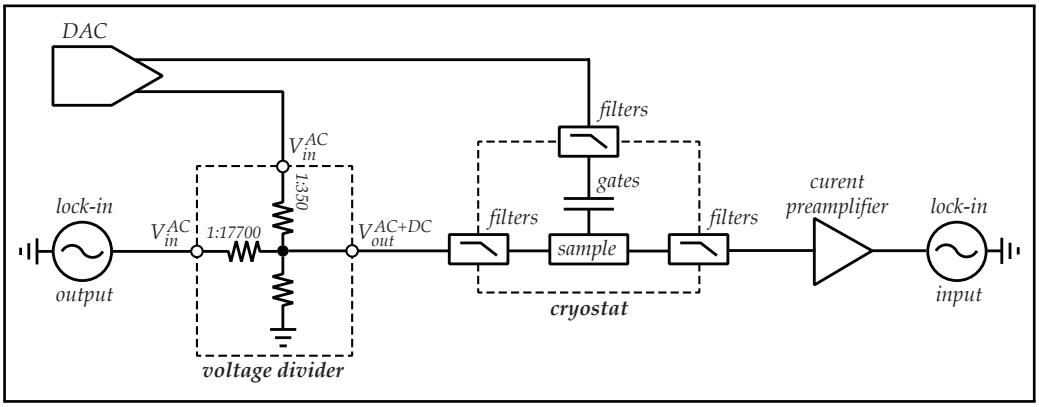

Figure 3.5: *Block diagram of the setup for device differential conductance measurements. The resolution of the applied AC, sourced from a lock-in, and DC, sourced from a DAC, voltage signal are enhanced by a voltage divider. Thereafter, the combined signal is filtered by a series of filters and applied to the sample. The generated AC current is preamplified and measured by the same lock-in. Digitally dividing the measured AC current by the applied AC voltage yields the conductance at the particular DC voltage. Measuring the conductance at different DC voltage values reveals the energy spectrum of the device. The DAC is also used to apply voltage to the gate electrodes capacitively coupled to the sample.*

measurements at different values of DC bias voltage reveals the device energy spectrum. Finally, the chemical potential of the sample can be locally altered by applying voltage, sourced from the same DAC, to gate electrodes.

Lithography is one of the most important tools for nanodevice fabrication. Exploiting electron beam with a controlled beam blanker one can pattern a chip with arbitrary electrical circuits in submicron scale. A well-established recipe is an essential ingredient in a successful fabrication. Following the recipe allows fabricating reproducible devices of good quality. The devices studied in this work are composed of semiconductor nanowires grown in molecular beam epitaxy chamber followed by epitaxial growth of half shell superconductor. After depositing individual wires on a chip, the superconductor is chemically removed for gating purposes. Next, the contacts and gates are patterned and metalized. Thereafter the devices are ready to be measured. In order to see phenomena related to quantum transport, the measurements are performed in a dilution refrigerator, which allows cooling the sample down to roughly 10 mK. The devices are characterized by utilizing standard AC lock-in techniques.

4

Majorana Hunting

Device geometry exploited in this work is one of the simplest geometries allowing nucleation and detection of Majorana zero modes, however, a few gate electrodes alongside the magnetic field exponentially increases the dimensionality of the tunable parameter space. Furthermore, every device is different and has its own character, which depends on every fine detail of fabrication, cool-down and even measurement itself. It soon becomes clear that the search for Majorana zero modes is rather an uneasy task. Nevertheless, there are several thumb rules, knowing of which can ease the device tuning into the topological regime. This chapter summarizes the gathered knowledge and main results of what in jargon is called 'Majorana hunting'.

4.1 Device of interest

In total four devices showing similar behavior have been investigated. The main texts is mainly concentrated on the device shown in Fig. 4.1, while the results from the three supplementary devices are summarized in Fig. A.1, A.2 and A.3 presented in the Appendix A.

Scanning electron micrograph in Fig. 4.1a reveals *N-I-S* geometry similar to the one mentioned in Section 2.10. The epitaxial hybrid nanowire segment of 2 µm in length serves as a superconducting lead. It is directly connected to the voltage source at one end and separated from a normal lead by a 100 nm constriction of bare semiconductor at the other one. The gate electrodes are placed on both sides of the device to increase their effectiveness. Each gate is shorted with its mirror counterpart to keep the applied electric potential in nanowire as constant as possible. A sharp pincher gate positioned at the constriction allows creating tunneling barrier, whereas the flat plunger gates

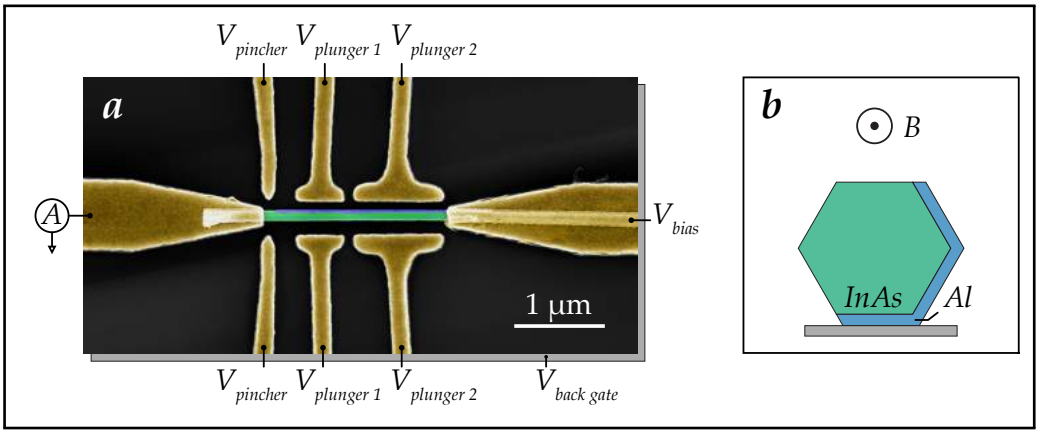

Figure 4.1: *Device of interest.* ***a:*** *Scanning electron micrograph of the device. The gold contacts are false colored in yellow, indium arsenide nanowire is colored in green, whereas the aluminum shell is colored in blue.* ***b:*** *Cross section of the nanowire indicating the Al half shell (blue) orientation with respect to the substrate (gray). The magnetic field, B, for the Majorana zero mode nucleation is applied parallel to the wire.*

are used to tune the chemical potential in the nanowire. In general, having two pairs of plunger gates, instead of a single one, enables a higher control of the system. Nevertheless, for the purpose of this work, the same voltage is applied to all the plungers, unless otherwise mentioned. Finally, the back side of the *Si* wafer serves as a powerful global back gate, applying voltage to which simultaneously tunes the strength of the tunneling barrier as well as the chemical potential of the wire. Sections 4.2 and 4.3 introduce the pincher and plunger gates, respectively, in more detail by demonstrating the effect of the applied voltage on the device conductance.

Schematic cross section of the nanowire is depicted in Fig. 4.1b. The relative orientation of *Al* half shell (blue) with respect to the substrate (gray) can result in several different configurations. This particular nanowire is placed on one of the *Al* covered facets, thus the back gate is expected to be less effective. Except otherwise specified, the magnetic field, *B*, is applied parallel to the *Al* shell and the nanowire using three-axis vector magnet. The role of the magnetic field orientation with respect to the wire is elaborated in more detail in section 4.4.

4.2 Pincher Gate

Applying voltage, $V_{pincher}$, to the pincher gate electrode, heightens the potential barrier at the constriction, hence reduces the device conductance. Increasing barrier gradually drives the electron transport through the junction

from transmission dominated to tunnelling dominated one. As argued in Section 2.8, spectroscopy performed in tunnelling regime reflects the density of states of the system, hence it is important to measure in a right region. Data illustrating the functionality of pincher gate (taken from the first supplementary, bottom gated device presented in Fig. A.1) is shown in Fig. 4.2.

Differential conductance, $\mathrm{d}I/\mathrm{d}V$, of the nanowire as a function of voltage applied to the pincher gate, $V_{pincher}$, versus the bias voltage, V_{bias}, between the normal and superconducting leads is depicted in 4.2a. As mentioned in section 3.4, the measurements are conducted in 2-terminal setup. As a result, in an open regime, that is at near to zero gate voltages, the measured voltage drop

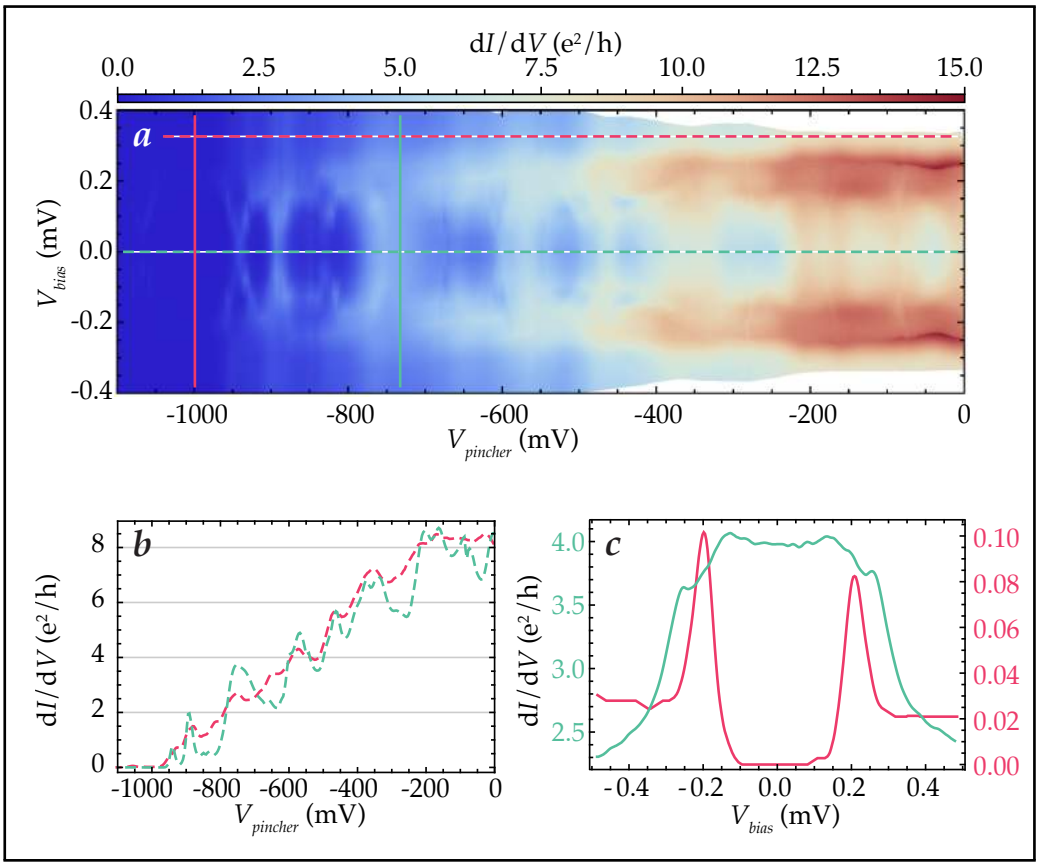

Figure 4.2: *Functionality of the pincher gate. Data taken from a device presented in Fig. A.1.* ***a:*** *Differential conductance of the device as a function of pincher gate and bias voltages.* ***b:*** *Line-cuts from* ***a*** *along $V_{pincher}$ displaying pinch-off curves at $V_{bias} = 0\,\mathrm{mV}$ (dashed green line) and $V_{bias} = 0.3\,\mathrm{mV}$ (dashed red line).* ***c:*** *Line-cuts from* ***a*** *along V_{bias} displaying conductance plateau at $V_{pincher} = -735\,\mathrm{mV}$ (solid green line) and tunneling regime at $V_{pincher} = -1000\,\mathrm{mV}$ (solid red line). Different axis scales are specified with corresponding colors.*

across the constriction is expected to be of similar order with the line resistance. This has been taken into the account by separately measuring the line resistance ($R_{line} \approx 750\,\text{Ohm}$) and subtracting it from the data.

One of the main features of the plot is that the more negative is $V_{pincher}$ the less conductive is the device. The subgap features crossing zero energy originate from a quantum dot in the constriction [48] and will be discussed in more depth in section 4.5. High conductance at zero gate voltage implies that several channels are open, whereas the transport is pinched-off completely at gate voltages bellow $V_{pincher} = -1000\,\text{mV}$. Increase in conductance at finite V_{bias}, both positive and negative, is noticeable throughout the whole conducting range of $V_{pincher}$. This feature is due to the presence of the Al shell. The magnitude of the induced superconducting gap, Δ^*, can be estimated from the distance between the two resonances in conductance which equals to $2\Delta^*/e$. The measured induced superconducting gap is found to be $\Delta^* \approx 0.21\,\text{mV}$. The value is comparable to the ones reported in similar epitaxial hybrid devices [48] and consistent with the values for evaporated ultra-thin Al films reported in Ref. [55,56]. Note that the induced gap in the device of interest is slightly higher ($\Delta^* \approx 0.25\,\text{mV}$, see for example Fig. 4.3a at $V_{plunger\,2} = -10\,000\,\text{mV}$).

The horizontal line cuts from Fig. 4.2a at $V_{bias} = 0\,\text{mV}$ and $0.3\,\text{mV}$ indicated by the dashed green and red lines, respectively, are plotted in Fig. 4.2b. The character of zero energy pinch-off curve is governed by the Coulomb peaks. Outside the gap, qualitative conductance quantization steps corresponding to the number of available channels can be perceived in the smoothened curve [57]. It is worth noting that the quantitative conductance quantization can only be observed in perfectly ballistic channels and so far has been reported in short devices only [58].

The vertical line cuts from Fig. 4.2a indicated by solid red and green lines at $V_{pincher} = -1000\,\text{mV}$ and $-735\,\text{mV}$, respectively, are plotted in Fig. 4.2c, note different axis scales specified by corresponding colors. Less conductive gate voltage (green line) reveals Andreev reflection-like conductance plateau. The conductance is twice the conductance quantum implying that the transport is mediated through two channels. In the tunneling regime (red line) the hard superconducting gap becomes apparent.

4.3 Plunger Gates

Due to the dimensional confinement in the nanowires, charge carriers can form standing waves. In general, both longitudinal and transverse modes are possible. For instance, a transverse wave can be bound between the bound-

aries to the superconductor on one side of the nanowire and vacuum on the other one. In a gross approximation, this process can be explained by an electron entering the nanowire and undergoing specular reflection at the boundary to the vacuum. The electron is then Andreev reflected at the boundary to the superconductor, hence a hole enters the nanowire and undergoes the same two reflection processes. The resulting bound stated is formed by the Andreev reflection and thus is termed Andreev bound state (ABS).

Usually, a wire with an unaltered density of states has multiple active bound states, making it difficult to interpret the measurements quantitatively. In order to address a single wire state, the others have to be depleted. This is normally done with the help of side plunger gates, see Fig. 4.1. Alternatively, one can also invoke the back gate for the task and adjust the tunneling barrier with the pincher gate accordingly.

Tunneling conductance, $\mathrm{d}I/\mathrm{d}V$, dependence on both plunger gate voltages, $V_{plunger\,2}$ and $V_{plunger\,1}$, separately as a function of bias voltage, V_{bias}, is shown in Fig. 4.3a and Fig. 4.3b, respectively. A higher-resolution version of Fig. 4.3b spanning a shorter range of $V_{plunger\,1}$ and showing a complex pattern is given in Fig. 4.3c. It is visible that both of the plunger gates affect the subgap states. However, from the scale it seems that $V_{plunger\,2}$ is less effective compared to $V_{plunger\,1}$. This suggests that either the subgap states are mostly localized near the constriction or they are simply not probed because they are too far from the tunneling barrier.

In addition to the subgap states, at energies above the superconducting gap, structures of Coulomb diamonds can be recognized. The charging energy, that is the height of the Coulomb diamonds, is at least a few mV, thus the corresponding quantum dot has to be small. The Coulomb blockade feature in the spectrum can be explained by the fact that there is a finite capacitive coupling between the end dot in the constriction and the plunger gates. Consequently, voltage applied to the plunger gates also affects the junction.

4.4 Magnetic Field Orientation

One of the main superconducting phase properties is that it expulses external magnetic fields, a phenomenon called Meissner effect [59]. The phenomenon is intimately related to the penetration depth explained by London [60], stating that even at zero temperature, external magnetic field strength decays exponentially as a function of distance from the surface. According to the Faraday's law, the change of the magnetic field generates current. Furthermore, as stated by the Ampère's law, any electric current induces a magnetic field. If

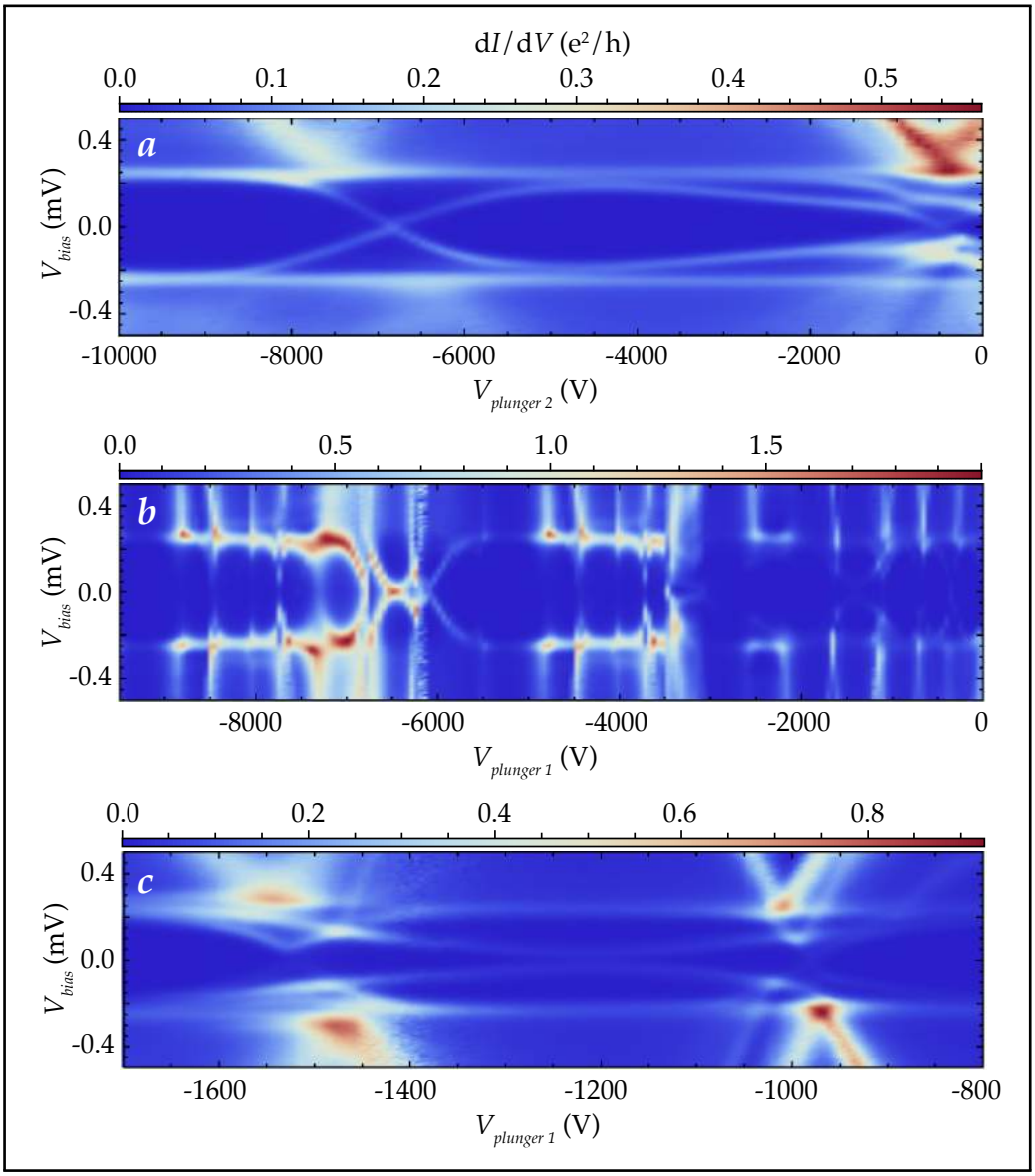

Figure 4.3: *Tunneling conductance spectra dependence on plunger gates.* ***a*** *&* ***b:*** *Device conductance dependence on $V_{plunger\,2}$ and $V_{plunger\,1}$ (see Fig. 4.1), respectively, as a function of V_{bias}.* ***c:*** *Higher resolution and smaller range version of* ***b*** *showing complex pattern. Plot* ***a*** *is measured at $V_{pincher} = -2000\,\mathrm{mV}$ and $V_{plunger\,1} = 0\,\mathrm{mV}$, whereas plots* ***b*** *and* ***c*** *are measured at $V_{pincher} = -2000\,\mathrm{mV}$ and $V_{plunger\,2} = -10\,000\,\mathrm{mV}$. Both of the gates tune subgap states, however, $V_{plunger1}$ has a bigger effect. Additionally, Coulomb diamonds are observable, which can be affiliated with the end dot, indicating finite coupling between the plunger gates and the junction.*

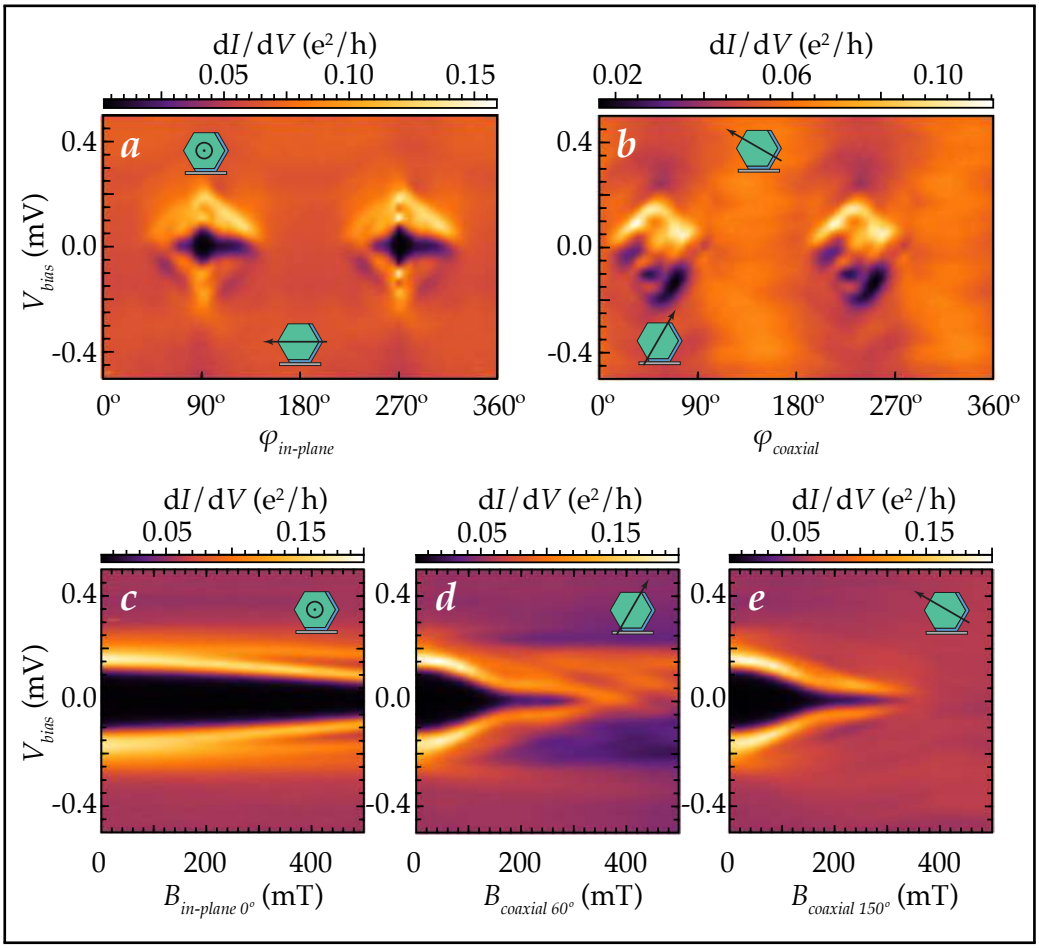

Figure 4.4: *Tunneling conductance dependence on the applied magnetic field orientation.* ***a & b:*** *Magnetic field with a fixed amplitude of* $|B| = 500\,\mathrm{mT}$ *is rotated in planes that are parallel to the substrate (in-plane) and perpendicular to the wire (coaxial), respectively. Insets indicate critical magnetic field orientations with respect to the Al shell and the substrate.* ***c-e:*** *Magnetic field amplitude sweeps along three critical directions indicated with corresponding insets. The data is taken at* $V_{pincher} = 1270\,\mathrm{mV}$, $V_{plunger1} = -3130\,\mathrm{mV}$, $V_{plunger2} = -10\,000\,\mathrm{mV}$ *and* $V_{back-gate} = -2000\,\mathrm{mV}$.

the external field is small, the generated current runs along the surface of the material, leaving the bulk superconducting. There is, however, a superconductor specific critical magnetic field, B_c, at which the generated current exceeds the maximum current a superconductor can carry and the material transits to a normal phase. For the samples with several symmetry axes, the magnitude of B_c depends on the external field orientation. In general, minimizing the penetration area maximizes the B_c.

Device conductance dependence on the external field orientation is summarized in Fig. 4.4. Both in-plane (parallel to the substrate) and coaxial (perpendicular to the wire) magnetic field rotations with a fixed amplitude of $|B| = 500\,\mathrm{mT}$ display two maxima, see Fig. 4.4a and 4.4b, respectively. The 180°-periodicity in both plots indicates two-fold symmetry, just as expected from the symmetry of the superconducting shell. Note that the 0° in both plots corresponds to the same magnetic field orientation, that is perpendicular to the wire and parallel to the substrate. The small insets indicate the magnetic field direction at critical points with respect to wire and substrate.

The maximum superconducting gap is obtained when the field is aligned parallel to the nanowire, see Fig. 4.4a, 90° and 180°. At the magnetic field aligned quasi-parallel to the *Al* shell, see 4.4b 60° and 240°, the envelope of superconducting gap is visible, however, the gap is filled with numerous quasicontinuous subgap states. This is because any non-parallel to the wire field will contribute to the Lorentz force enhancing by the orbital physics induced band bending. Furthermore, only to the spin-orbit field perpendicular component of the external magnetic field contributes to the spin band mixing and Zeeman splitting required for the topological phase, see section 2.6. Since the Rashba spin-orbit field is perpendicular to the direction of charge carrier motion, the gap is maximized when the external field is parallel to the wire.

Magnetic field amplitude sweeps along three critical orientations are presented in Fig. 4.4c-e. In case of parallel to the wire magnetic field, see Fig. 4.4c, superconducting gap is preserved over the whole measured range. A single subgap state slowly approaching zero energy is visible. Quasi-parallel to the *Al* shell, but perpendicular to the wire oriented magnetic field, see see Fig. 4.4d, completely fills the gap with states over the first few 100 mT, however, the feature of superconductivity persist over the whole range. Lastly, no clear signature of superconducting gap above 300 mT is visible in case of the field oriented perpendicular to both wire and superconducting shell, see Fig. 4.4e.

4.5 Understanding the Device

After getting acquainted with all the tunable knobs, one can continue with device study. As mentioned in Section 4.2 an unintentional quantum dot is formed at the junction between the normal and superconducting leads due to disorder or band bending [48]. Differential conductance, $\mathrm{d}I/\mathrm{d}V$, as a function of $V_{pincher}$ and V_{bias} spanning three Coulomb valleys is shown in Fig. 4.5a. Linear extrapolation of the Coulomb peak maxima yields the height (in V_{bias}) of the Coulomb blockade diamond and reveals the charging energy $E_C \approx 4.5\,\mathrm{meV}$ of

the end dot.

The reported charging energy is much larger than the induced superconducting gap $E_C \gg \Delta^*$. As a result, parking $V_{pincher}$ in the middle of a Coulomb valley brings the discrete quantum dot levels far away from the resonant peaks

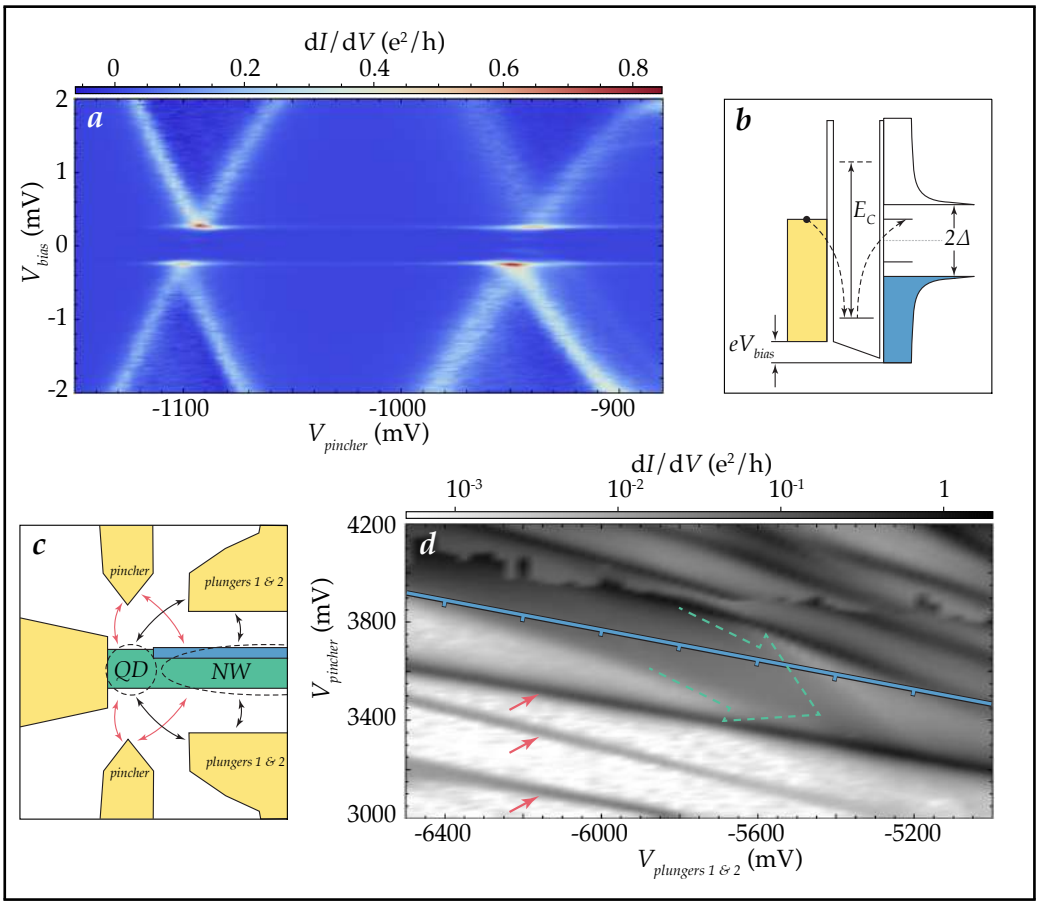

Figure 4.5: ***a:*** *Device conductance as a function of $V_{pincher}$ and V_{bias}, displays to the quantum dot characteristic Coulomb diamonds, the height of which correspond to the dot charging energy of $E_c = 4.5\,\mathrm{meV}$. The data is taken at $V_{plungers\,1\,\&\,2} = -7200\,\mathrm{mV}$ and $V_{back-gate} = -2000\,\mathrm{mV}$.* ***b:*** *The dot charging energy is much higher than the induced superconducting gap. Therefore cotunneling processes dominate the transport in the Coulomb blockade regime.* ***c:*** *A schematic of device shown in Fig. 4.1a illustrating the capacitive coupling between the gates and both the quantum dot (QD) and the nanowire (NW).* ***d:*** *Conductance of the device as a function of $V_{plungers\,1\,\&\,2}$ and $V_{pincher}$ measured at $V_{bias} = 0\,\mathrm{mV}$, $V_{back-gate} = -8000\,\mathrm{mV}$ and $B = 1000\,\mathrm{mT}$. Note tha logarithmic color scaling. The sharp states indicated by red arrows correspond to the Coulomb blockade peaks of the end dot, whereas the broad state is assigned to the wire state.*

of the induced superconducting gap, see Fig. 4.5b. In this scenario, the transport is mediated via single electron cotunneling and the dot effectively acts as a tunneling barrier, allowing to probe the wire. As mentioned in Section 4.3, the end dot has a finite coupling to the plunger gates, thus tuning the wire states with $V_{plungers\ 1\ \&\ 2}$ simultaneously influences the states of quantum dot. Similarly, change in $V_{pincher}$ has a finite impact on the wire states. The capacitive cross coupling of the gate electrodes is illustrated in Fig. 4.5c.

Differential conductance of the device as a function of combined plunger 1 & 2 gate voltage, $V_{plungers\ 1\ \&\ 2}$, and pincher gate voltage, $V_{pincher}$, measured at $V_{bias} = 0\,\mathrm{mV}$ and $B = 1000\,\mathrm{mT}$ is shown in Fig. 4.5d. The sharp states, indicated by red arrows, are more sensitive to the $V_{pincher}$, hence assigned to the Coulomb peaks of the end dot. The state indicated with a dashed green arrow is broader and lower in intensity, and has a relatively higher response to $V_{plungers\ 1\ \&\ 2}$, therefore it is attributed to the wire state pulled down to zero energy by the strong magnetic field. The switching character at $V_{pincher} \approx 4000\,\mathrm{mV}$ is assigned to a disorder. It appears to be stable and thus can be avoided. Cotunneling spectroscopy of the wire states through the Coulomb blockade valley independent from the dot states can be carried out by following the iso-potential line of the end dot indicated in blue. For this the plunger gates ($V_{plungers\ 1\ \&\ 2}$) have to be compensated with the pincher gate ($V_{pincher}$) by the ratio determined from the slope of the dot state.

It is worth pointing out, that the superconducting lead of the device is grounded, thus its charging energy is zero. Because it is smaller than the superconducting gap, the wire states will not change their parity at $B = 0\,\mathrm{mT}$. At a finite magnetic field, however, the wire states experience Zeeman splitting, which eventually brings the states down to zero energy. In a trivial phase, after crossing zero energy the ABSs reopens again, which can be understood as a fermion parity change. In the topological phase, on the other hand, the ABSs merge and stay pinned down to zero over a large range of magnetic field. The robust zero energy states can be interpreted as a formation of MZMs, which due to their origin are also termed Majorana bound states (MBS) [61, 62].

4.6 Majorana Identification

After the excursion in parameter space, the stage is set for the hunt of the elusive Majorana particles. The strongest signature of a captured Majorana mode in the DC transport measurements, although not conclusive, is a zero bias peak persisting over a large range of an applied magnetic field. The indisputable evidence of the Majorana quasiparticle existence would be the demonstration

of their exotic non-Abelian exchange statistics [46]. That being said, presently there is no other known mechanism besides MBSs, which would explain the collection of results presented bellow.

It is difficult to get hold of the topological regime by simply sweeping the magnetic field at a randomly fixed gate configuration. More efficient approach is to characterize a specific gate region by measuring wire chemical potential dependence of the device tunneling spectrum at a few different magnetic field values. Figures 4.6a-d display subgap state evolution in gate voltage ($V_{compensated\ plungers}$) swept along the blue line in Fig. 4.5d at $B = 0\,\mathrm{mT}$, $400\,\mathrm{mT}$, $1000\,\mathrm{mT}$ and $1600\,\mathrm{mT}$, respectively. At zero field, see Fig. 4.6a, multiple ABSs are visible with minimum energy $\zeta \approx 0.08\,\mathrm{meV}$ smaller than the effective superconducting gap $\Delta^* \approx 0.25\,\mathrm{meV}$. The states are interpreted as confinement-induced longitudinal modes from a single transverse subband [63]. The particle-hole symmetry is reflected in the around zero energy symmetric spectra. Turning on the magnetic field starts to mix states [64], see Fig. 4.6b, and introduces anticrossings between adjacent parabolas [65]. Increasing magnetic field further pulls the state to zero energy, see Fig. 4.6c. Topological regime becomes evident, once the Zeeman energy exceed the superconducting gap: a robust zero bias peak persist over a finite interval of $V_{compensated\ plungers}$, see Fig. 4.6d.

Finally, the topological phase can be investigated by taking magnetic field cuts at several different gate configurations. Subgap state dependence on the magnetic field at different gate configurations is shown in Fig. 4.7. Evolution of the ABSs with the lowest energy at gate voltage marked by a square in Fig. 4.6 can be tracked in Fig. 4.7. The states are quick to reach zero and merge already at 500 mT. Note that there is no visible state mixing at low field. After enduring at zero energy for several 100 mT, the states split again at roughly 1300 mT. Lastly, the states merge with the higher energy ABSs above 1600 mT. Similar behavior has been reported in Refs. [66], that is at the border to the topological regime. The ABSs evolve qualitatively different where two modes overlap at zero field. The corresponding magnetic field cut at gate voltage marked by a triangle in Fig. 4.6 is given in Fig. 4.7b. After mixing and splitting at low field, the lowest energy ABSs merge and give rise to robust zero bias peak continuing from 700 mT up to 2000 mT. At more negative gate voltage marked by a circle in Fig. 4.6, one runs into another pair of ABSs. Corresponding magnetic field sweep shown in Fig. 4.7c also displays a zero bias peak forming at a slightly higher magnetic field (≈850 mT) and vanishing into the background at the end of the measured range. This behavior suggests that there should be a nearby phase transition back to the trivial phase.

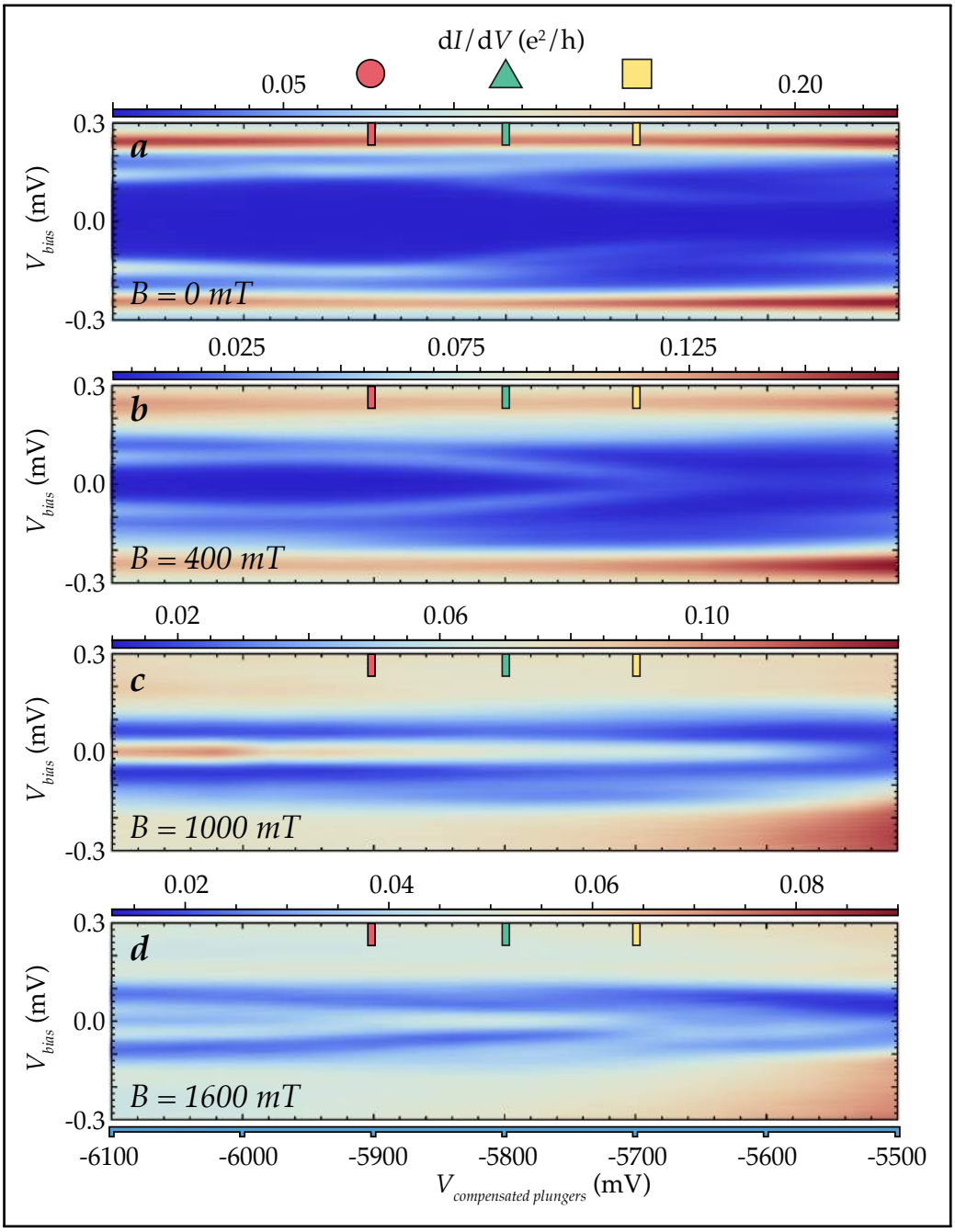

Figure 4.6: *Wire chemical potential dependence of subgap states.* ***a to d:*** *Differential tunneling conductance as a function of compensated plunger gate voltage along the blue line in Fig. 4.5, $V_{compensated\ plungers}$, and bias voltage V_{bias} at $B = 0\,\mathrm{mT},\ 400\,\mathrm{mT},\ 1000\,\mathrm{mT}$ and $1600\,\mathrm{mT}$, respectively.*

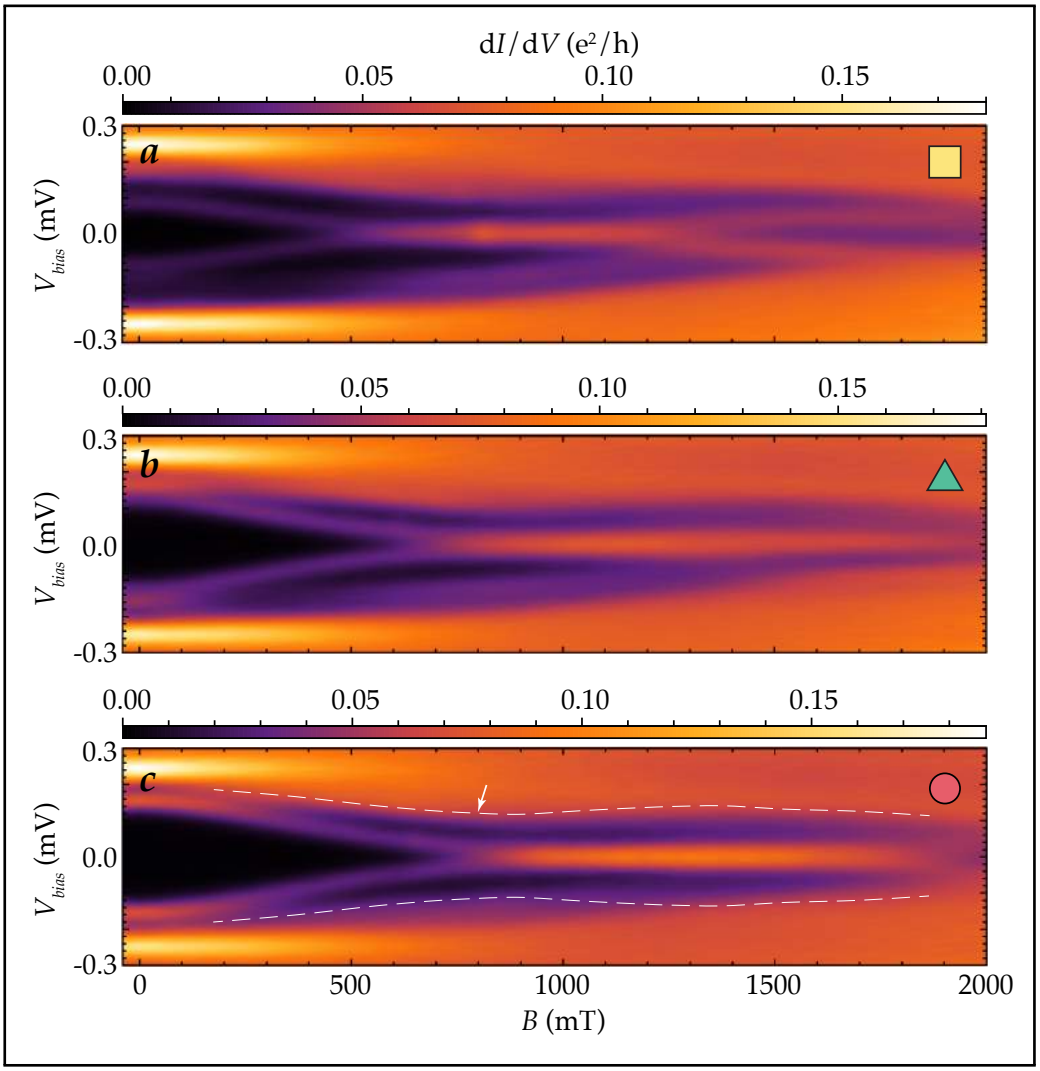

Figure 4.7: *Magnetic field dependence of subgap states.* ***a to c:*** *The cuts are done at gate voltages indicated by the square, triangle and circle in Fig. 4.6, respectively. Depending on the different gate configurations, the evolution of ABSs display different behavior. The dashed white line in* ***c*** *is a guide for the eye marking the evolution of the first excited ABSs, observable in all three sweeps. The white arrow indicates the topological phase transition.*

The first excited pairs of ABSs in all three sweeps (for clearness indicated by dashed white lines in Fig. 4.7c) qualitatively resembles the behavior described in Ref. [63]. First of all, they are pulled down towards zero energy, but then they bounce back up at approximately where the lowest energy pair of ABSs merge together (signified by a white arrow in Fig. 4.7c). This signature is the manifestation of the finite nanowire length and is interpreted as the phase

transition to the topologically nontrivial state. The further evolution of the first excited states is dominantly governed by the collapse of the superconducting gap. The closing of the trivial and opening of the topological gap, with a single discrete state with the zero energy extended over a long range of magnetic field is understood as the formation of MBSs localized at the ends of the wire.

Finding the topological phase and Majorana quasiparticles within is a task that requires some knowledge and experience. Understanding the investigated device and following a goal-directed protocol is essential. In order not to get lost in the vast parameter space, one should get acquainted with the device response to the tunable knobs. The device investigated in this work is of *N-I-S* geometry, see Fig. 4.1, where *N* is a normal lead separated from a proximitized nanowire serving as superconducting lead *S* by a semiconducting constriction *I*. Tunneling spectroscopy of the epitaxial hybrid nanowire density of states can be performed by applying voltage to the so-called pincher gate, thus creating a tunneling barrier in the constriction, see Fig. 4.2. Due to the spatial confinement, the nanowire tends to form Andreev reflection induced bound states, the density of states of which can be tuned with plunger gate electrodes as shown in Fig. 4.3. Magnetic field plays a key role in the search of the Majorana excitations. The significance of the applied magnetic field orientation is summarized in Fig. 4.4. Additionally, a quantum dot is formed in the constriction, presumably because of the band bending or disorder. The charging energy of the dot is found to be much larger ($E_c \approx 4.5\,\mathrm{meV}$) than the induced superconducting gap ($\Delta^* \approx 0.25\,\mathrm{meV}$), thus keeping it off resonance allows to use it as a spectrometer, see Fig. 4.5. Taking snapshots of tunneling spectrum dependence on wire chemical potential at several different magnetic field values helps to roughly locate the topological phase in the gate space, see Fig. 4.6. Finally, the formation of Majorana bound states from coalescing Andreev bound states can be recorded by sweeping the magnetic field at an appropriate gate configuration.

5

Epilogue

The writing is finalized by shortly summing up the highlights of this work and giving a quick outlook into the next generation experiment.

5.1 Summary

Majorana excitations in condensed matter are fascinating from fundamental as well as from application point of view [15]. Due to their topological nature, the quasiparticles are immune against most types of decoherence [8]. Furthermore, the particles obey exotic non-Abelian statistics, therefore are excellent candidates for topological qubit implementation [7]. First experiments based on series of theoretical proposals [19,26,27] allowed detecting zero energy state, which was interpreted as Majorana zero modes [39]. Additional experiments further confirmed the result and deepened the understanding of the Majorana modes [40,49,50]. Nevertheless, the origin of the quasiparticles remained obscure. The present work sheds some light on the matter by introducing the step-by-step protocol of Majorana hunting. Detection of the topological phase extended in gate voltage and magnetic field space is demonstrated. Finally, it is shown that Majorana bound states emerge from coalescing confinement induced Andreev bound states.

5.2 Outlook

As specified above, a conclusive proof of Majorana quasiparticle existence is the verification of non-Abelian statistics. As explained in Ref. [46], this can be done in branched geometries applying fast gate operations. This is a challenging experiment and requires joint forces from several different fields

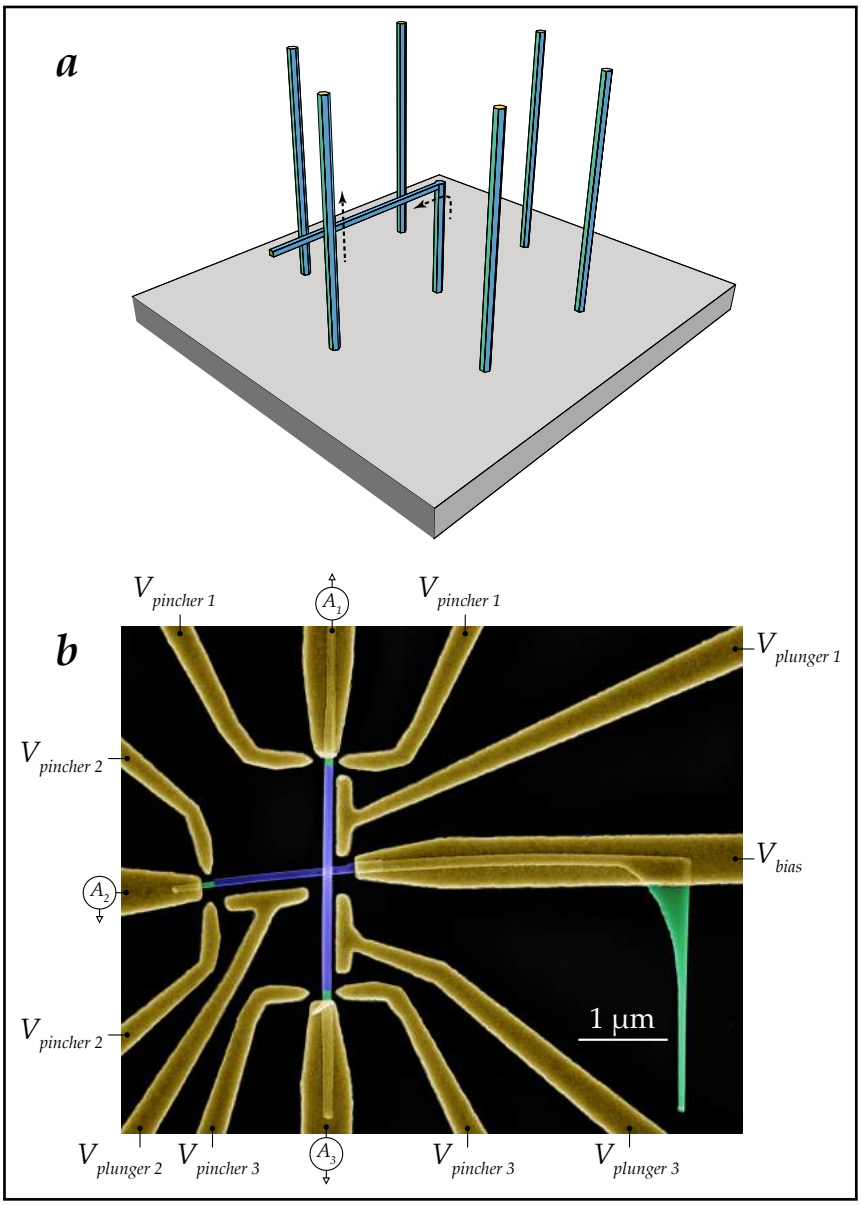

Figure 5.1: *Outlook for the second generation devices.* ***a:*** *In hexagonal manner prepared gold (gold) seed particles acts as catalyst in the semiconductor nanowire (green) growth using molecular beam epitaxy technique. By changing the growth conditions can cause arbitrary kinking of the wires. Due to the crystal symmetry the kinked wires continue growing parallel to the substrate in one out of six possible directions and eventually merge with the unkinked wire forming a cross. Epitaxial aluminum (blue) is deposited on the grown wires.* ***b:*** *Scanning electron micrograph of the second generation device. One out of four ends serves as a source, whereas the other ends are used as drains allowing to perform spectroscopy at each branch separately.*

of physics. High-quality nanowire networks are required, therefore material science plays a very important role. One of the possible implementations is presented in Fig. 5.1.

Nanowire growth is seeded with gold catalyst particles, which are pre-patterned on the wafer in a hexagonal manner using electron beam lithography, see Fig. 5.1b. Changing growth conditions makes the gold droplet sitting on top of the wire shift to the edge. Due to the crystal symmetry, the nanowires continue the growth parallel to the substrate in one out of six possible directions. The kinked nanowire eventually hits one of the neighboring unkinked wires, hence forming a cross. The wire growth is followed by low temperature angled epitaxial aluminum deposition.

A scanning electron micrograph of the second generation device is depicted in Fig. 5.1b. One out of four branches is sourced with a bias voltage, while tunneling conductance of the rest three branches can be probed separately. Demonstrating Majorana quasiparticles at all three ends would prove the concept of branched devices, opening the doors for the ultimate braiding experiment.

A

Appendix

In addition to the device studied in the main text, three other devices have been investigated, two of which were bottom gated. To prevent the device from shorting, the bottom gates are covered with an insulating oxide layer fabricated using atomic layer deposition (ALD) technique. Using bottom gates is a trade-off between stronger gates (because of the smaller spacing and higher dielectric constant material) and charge traps induced hysteresis (because of impure growth). Furthermore, wire deposition requires higher mental focus. Nevertheless, careful fabrication might yield device offering high degrees of chemical potential control. The two-step lithography is carried out on the blank chips, thereafter the further device fabrication is finalized as described in the main text.

- For the first step, 950kPMMA A2 electron beam resist is spun and baked at 115 °C for 120 sec. Thin resist is chosen for sharp features.
- The bottom gate pattern is exposed with 240 000 px per 600 µm resolution, 800 $\frac{\mu C}{cm^2}$ dose & 500 pA beam current. It is important not to overexpose the fine pattern, otherwise the gates might get shorted.
- The chip is then developed and cleaned with plasma as usually.
- The gates are metalized with
  - 5 nm of *Ti* with 0° tilt and 45 rpm rotation;
  - 15 nm of *Au* with 0° tilt and 45 rpm rotation;
- The step is completed by the lift-off.
- For the second step, a bi-layer of MMA EL13 + 950kPMMA A4 electron beam resist is spun and baked (each layer) at 115 °C for 120 sec.
- The windows for ALD oxide are exposed with 240 000 px per 600 µm resolution, 1280 $\frac{\mu C}{cm^2}$ dose & 500 pA beam current. Here, it does not really matter if the resist gets over exposed therefore a higher does is chosen to

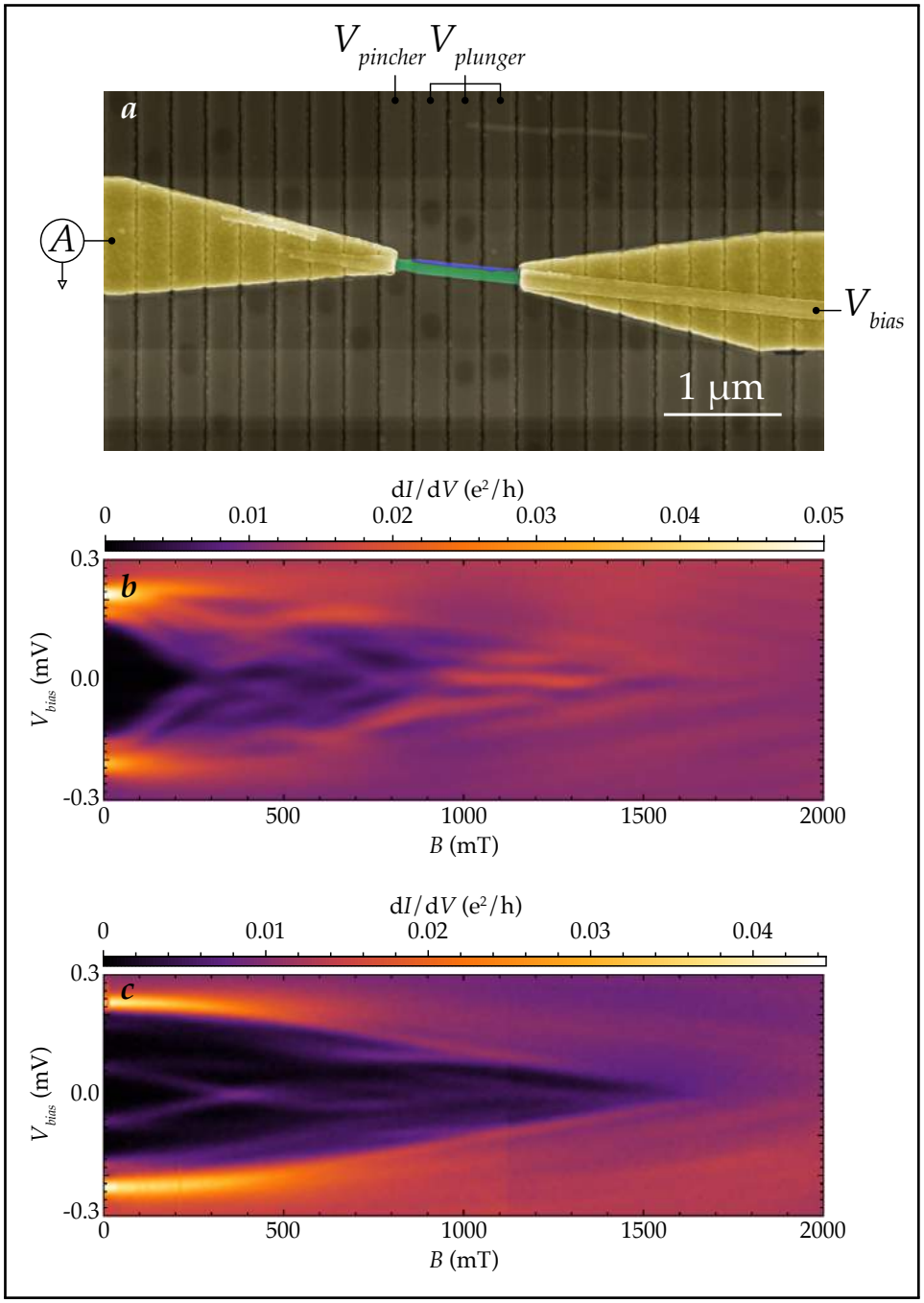

Figure A.1: *The first supplementary device.* ***a:*** *Scanning electron micrograph of the (bottom gated) device.* ***b and c:*** *Differential tunneling conductance, dI/dV, as a function of magnetic field, B, and bias voltage, V_{bias}. The graph in* ***b*** *is measured at $V_{plunger} = 0\,\mathrm{mV}$ and $V_{pincher} = -1120\,\mathrm{mV}$ and displays quasi-continuous band of wire states. The graph in* ***c*** *is recorded at $V_{plunger} = -6000\,\mathrm{mV}$ and $V_{pincher} = -950\,\mathrm{mV}$ and displays only a few discrete wire states.*

be on the safe side.
- The chip is then developed and cleaned with plasma.
- The insulating layer of Hafnium (Hf) oxide is deposited by 130 cycles (1 cycle $\approx$1 Å) of
  - 0.4 sec pulse of Hf-based precursor followed by 100 sec adsorption;
  - 0.03 sec pulse of water followed by 300 sec purging;
- In order to ease up the lift-off, the chip is scratched at the corners with a soft needle.
- The lift-off is carried out by dunking the chip into glass beaker with NMP at 80 °C for roughly an hour and then sonicating at 80 kHz with 100 % power for around 4 min.

The device shown in A.1a is used to demonstrate the functionality of the pincher gate in Section 4.2. Additionally, the control of wire density of states is demonstrated subgap state evolution in magnetic field, B, at different plunger gate voltages, $V_{plunger}$, see Figs. A.1b and c. The former graph shows device tunneling conductance, $\mathrm{d}I/\mathrm{d}V$, as a function of magnetic field, B, applied parallel to the wire and bias voltage, V_{bias}, at $V_{plunger} = 0\,\mathrm{mV}$ and $V_{pincher} = -1120\,\mathrm{mV}$. A cluster of wire states fill the gap already at a few 100 mT making it difficult to address the individual states separately. The later graph is taken at $V_{plunger} = -6000\,\mathrm{mV}$ and $V_{pincher} = -950\,\mathrm{mV}$ and exhibits quite different behavior: only a few discrete states are present within the gap, the evolution of which can easily be followed.

Two supplementary devices showing qualitatively similar behavior to the device discussed in the main text are summarized in Figs. A.2 and A.3. The figures are structured as follows: panel a displays false colored device scanning electron micrograph; panel b shows the wire chemical potential (at constant quantum dot potential) dependence of the subgap states at finite magnetic field; panel c shows subgap state evolution in magnetic field at the gate voltage marked by the triangle in panel b. Both devices display ABSs coalescing into a robust zero energy state at a finite magnetic field, which are interpreted as MBSs. The eye shaped re-splitting and re-merging at around 1100 mT in Fig. A.3c is attributed to the confinement-induced quantization effects discussed in Ref. [63].

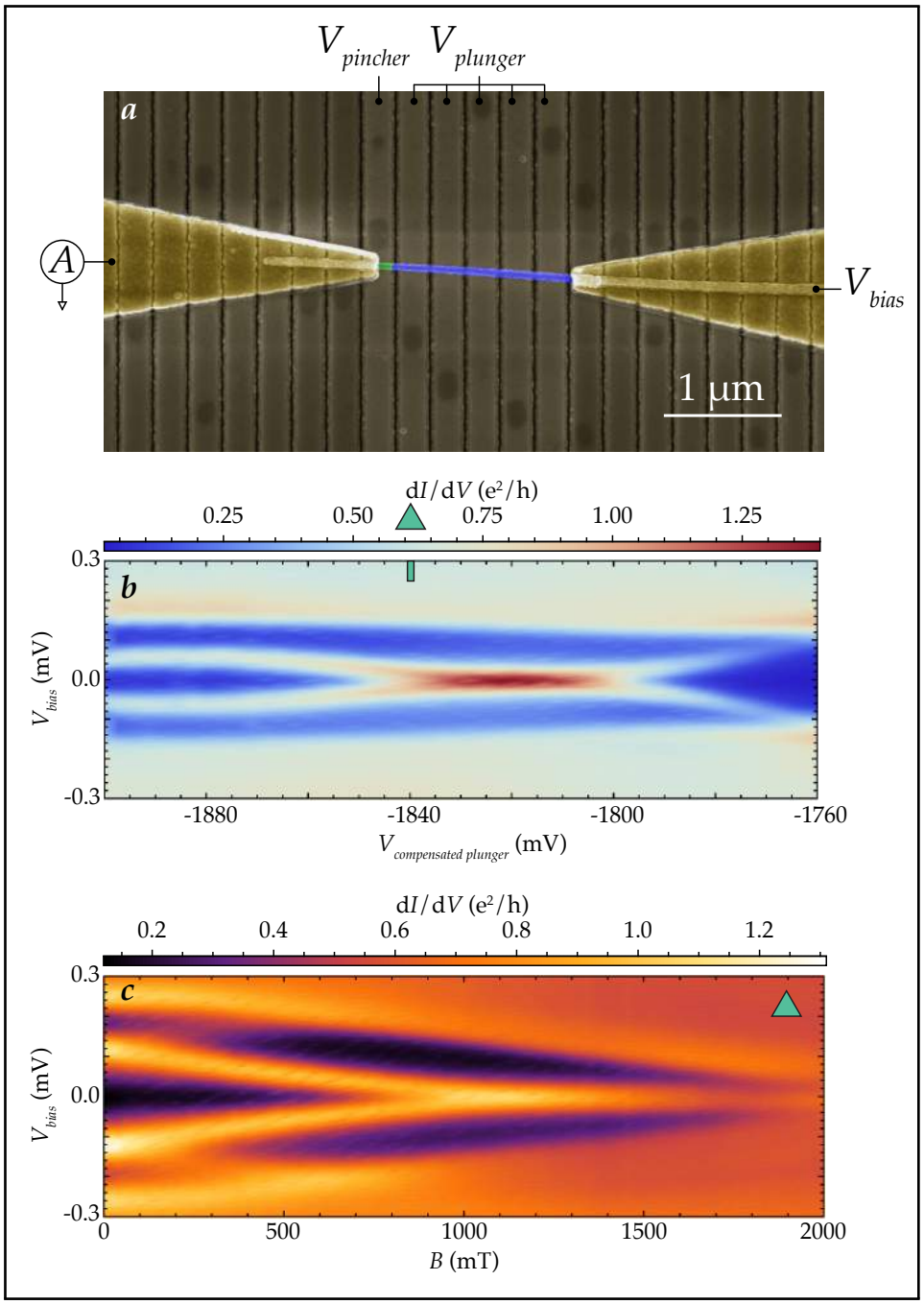

Figure A.2: *The second supplementary device.* ***a:*** *Scanning electron micrograph of the (bottom gated) device.* ***b:*** *Wire chemical potential dependence of the subgap states taken at* $B = 1000\,\mathrm{mT}$. ***c:*** *Magnetic field dependence of the subgap states taken at* $V_{plunger} = -1840\,\mathrm{mV}$ *and* $V_{pincher} = -609\,\mathrm{mV}$.

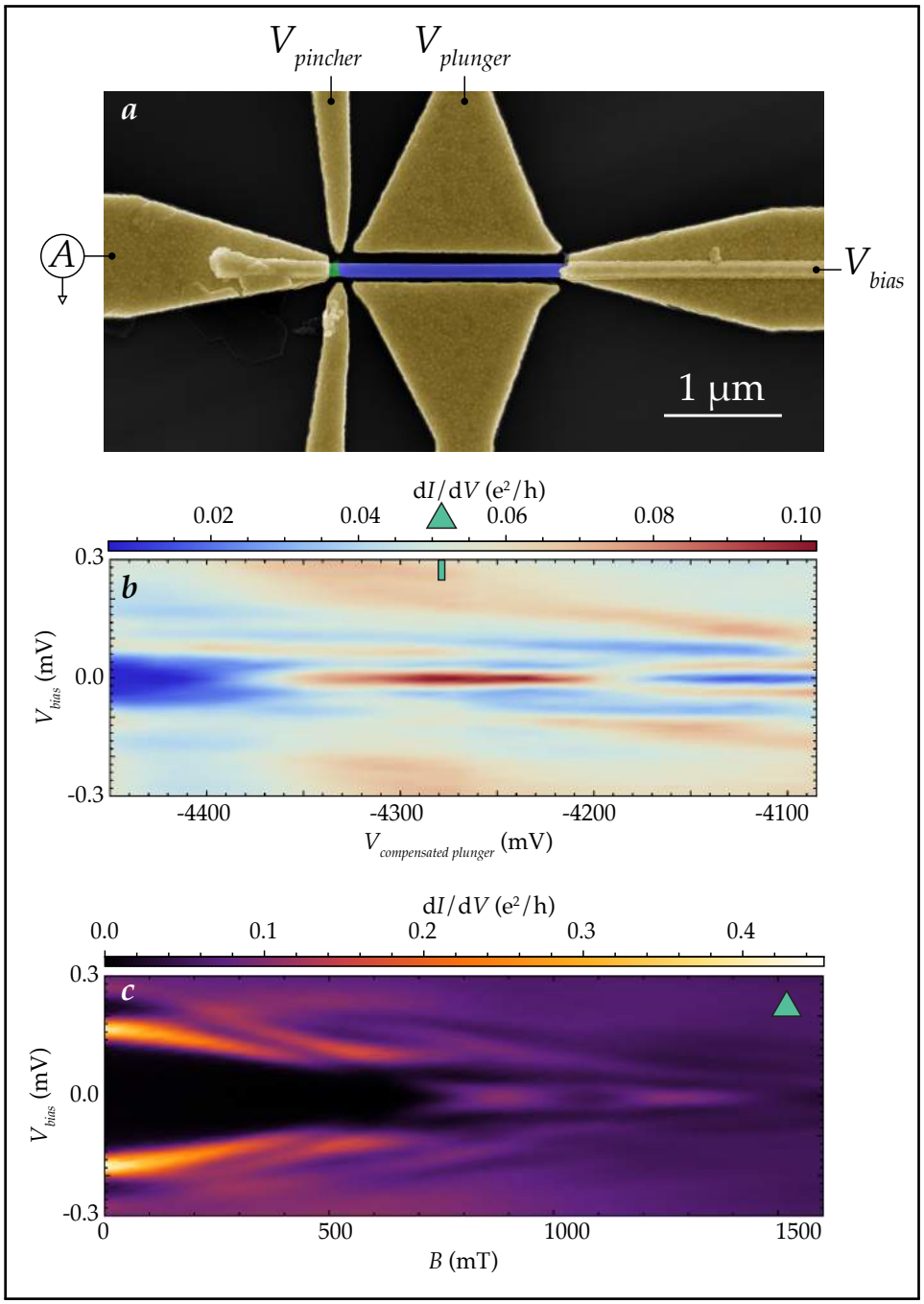

Figure A.3: *The third supplementary device.* ***a:*** *Scanning electron micrograph of the (side gated) device.* ***b:*** *Wire chemical potential dependence of the subgap states taken at* $B = 1200\,\mathrm{mT}$. ***c:*** *Magnetic field dependence of the subgap states taken at* $V_{plunger} = -4278\,\mathrm{mV}$ *and* $V_{pincher} = -3221\,\mathrm{mV}$.

References

[1] G. E. Moore, "Cramming More Components onto Integrated Circuits", *Electronics*, 114-117 (1965).

[2] R. P. Feynman, "Quantum Mechanical Computers", *Opt. News*, **11**, 11-20 (1985).

[3] D. P. DiVincenzo, "Topics in Quantum Computers", *arXiv:cond-mat/9612126* (1996).

[4] P. W. Shor, "Scheme for reducing decoherence in quantum computer memory", *Phys. Rev. A*, **52**, R2493(R) (1995).

[5] S. Das Sarma, M. Freedman and C. Nayak, "Topological quantum computation", *Physics Today*, 32-38 (2006).

[6] D. Epelbaum and R. Lorgat, "Computation in a Topological Quantum Field Theory", `http://www.scottaaronson.com/6s899/raeezlorgat-danielepelbaum.pdf` (2015).

[7] A. Y. Kitaev, "Fault-tolerant quantum computation by anyons", translated and reprinted in: *Annals Phys.*, **303**, 2-30 (2003).

[8] M. Leijnse and K. Flensberg, "Introduction to topological superconductivity and Majorana fermions", *Semicond. Sci. Technol.*, **27**, 124003 (2012).

[9] P. A. M. Dirac, "The quantum theory of the electron", *Proceedings of the Royal Society of London A: Mathematical, Physical and Engineering Sciences*, **117**, 610-624 (1928).

[10] C. D. Anderson, "The positive electron", *Physical Review*, **43**, 6, 491 (1933).

[11] E. Majorana, "Teoria simmetrica dell'elettrone e del positrone," *Nuovo Cimento*, **14**, 171-184 (1937).

[12] F. Wilczek, "Majorana returns", *Nature Physics*, **5**, 614-618 (2009).

[13] G. Moore and N. Read, "Nonabelions in the fractional quantum hall effect", *Nuclear Physics B*, **360**, 362-396 (1991).

[14] J. R. Schrieffer, "Theory of Superconductivity", *W. A. Benjamin* (1964).

[15] S. Das Sarma, M. Freedman and C. Nayak, "Majorana zero modes and topological quantum computation", *npj Quantum Information*, **1**, 15001 (2015).

[16] A. Kitaev, "Anyons in an exactly solved model and beyond", *Ann. Phys.*, **321**, 2-111 (2006).

[17] C. Nayak, S. H. Simon, A. Stern, M. Freedman and S. Das Sarma, "Non-Abelian anyons and topological quantum computation", *Rev. Mod. Phys.*, **80**, 1083-1159 (2008).

[18] D. A. Ivanov, "Non-Abelian statistics of half-quantum vortices in p-wave superconductors", *Phys. Rev. Lett.*, **86**, 268-271 (2001).

[19] A. Yu Kitaev, "Unpaired Majorana fermions in quantum wires", *Usp. Fiz. Nauk.*, **171**, 131-136 (2001).

[20] J. Alicea, Y. Oreg, G. Refael, F. von Oppen and M. P. A. Fisher, "Non-Abelian statistics and topological quantum information processing in 1D wire networks", *Nat. Phys.*, **7**, 412-417 (2011).

[21] S. Das Sarma, Jay D. Sau and T. D. Stanescu, "Splitting of the zero-bias conductance peak as smoking gun evidence for the existence of the Majorana mode in a superconductor-semiconductor nanowire", *Phys. Rev. B*, **86**, 220506(R) (2012).

[22] M. M. Salomaa, G. E. Volovik, "Half-Quantum Vortices in Superfluid He3-A", *Phys. Rev. Lett.*, **55**, 1184-1187 (1985).

[23] A. P. Mackenzie, Y. Maeno, "The superconductivity of Sr2RuO4 and the physics of spin-triplet pairing", *Rev. Mod. Phys.*, **75**, 657-712 (2003).

[24] L. Fu and C. L. Kane, "Superconducting Proximity Effect and Majorana Fermions at the Surface of a Topological Insulator", *Phys. Rev. Lett.*, **100**, 096407 (2008).

[25] P. G. de Gennes, "Boundary Effects in Superconductors", *Rev. Mod. Phys.*, **36**, 225 (1964).

[26] R. M. Lutchyn, J. D. Sau and S. D. Sarma, "Majorana Fermions and a Topological Phase Transition in Semiconductor-Superconductor Heterostructures", *Phys. Rev. Lett.*, **105**, 077001 (2010).

[27] Y. Oreg, G. Rafael and F. von Oppen, "Helical Liquids and Majorana Bound States in Quantum Wires", *Phys. Rev. Lett.*, **105**, 177002 (2010).

[28] A. F. Andreev, "The Thermal Conductivity of the Intermediate State in Superconductors", *Soviet Physics Jetp*, **19**, 5, 1228-1231 (1964).

[29] G. E. Blonder, M. Tinkham and T. Klapwijk, "Transition from metallic to tunneling regimes in superconducting microconstrictions: Excess current, charge imbalance, and supercurrent conversion", *Phys. Rev. B*, **25**, 4515-4532 (1982).

[30] A. V. Zaitsev, "Quasiclassical equations of the theory of superconductivity for contiguous metals and the properties of constricted microcontacts", *JETP Letters*, **86**, 1742-1758 (1984).

[31] G. B. Arnold, "Superconducting Tunneling Without the Tunneling Hamiltonian", *Journal of Low Temperature Physics*, **59**, 1-2, 143-183 (1985).

[32] R. Landauer, "Spatial Variation of Currents and Fields Due to Localized Scatterers in Metallic Conduction", *IBM Journal of Research and Development*, **1**, 223-231 (1957).

[33] T. M. Klapwijk, "Proximity Effect From an Andreev Perspective", *Journal of Superconductivity*, **17**, 593-611 (2004).

[34] P. G. de Gennes and D. Saint-James, "Elementary excitations in the vicinity of a normal metal-superconducting metal contact", *Phys. Lett.*, **4**, 151 (1963).

[35] C. R. Reeg and D. L. Maslov, "Hard gap in a normal layer coupled to a superconductor", *Phys. Rev. B*, **94**, 020501(R) (2016).

[36] K. Neurohr, A. A. Golubov, T. Klocke, J. Kaufmann, T. Schäpers, J. Appenzeller, D. Uhlisch, A. V. Ustinov, M. Hollfelder, H. Lüth and A. I. Braginski, "Properties of lateral Nb contacts to a two-dimensional electron gas in an $In_{0.77}$ $Ga_{0.23}As$/InP heterostructure", *Phys. Rev. B*, **54**, 17018 (1996).

[37] A. Chrestin, T. Matsuyama and U. Merkt, "Evidence for a proximity-induced energy gap in Nb/InAs/Nb junctions", *Phys. Rev. B*, **55**, 8457 (1997).

[38] B. A. Aminov, A. A. Golubov, M. Yu. Kupriyanov, "Quasiparticle current in ballistic constrictions with finite transparencies of interfaces", *Phys. Rev. B*, **53**, 365 (1996).

[39] V. Mourik, K. Zuo, S. M. Frolov, S. R. Plissard, E. P. A. M. Bakkers, L. P. Kouwenhoven, "Signatures of Majorana Fermions in Hybrid Superconductor-Semiconductor Nanowire Devices", *Science*, **336**, (6084), 1003 (2012).

[40] M. T. Deng, C. L. Yu, G. Y. Huang, M. Larsson, P. Caroff and H. Q. Xu, "Anomalous Zero-Bias Conductance Peak in a Nb-InSb Nanowire-Nb Hybrid Device", *Nano Lett.*, **12**, 6414-6419 (2012).

[41] L. P. Rokhinson, X. Liu and J. K. Furdyna, "The fractional a.c. Josephson effect in a semiconductor-superconductor nanowire as a signature of Majorana particles", *Nature Physics*, **8**, 795-799 (2012).

[42] A. D. K. Finck, D. J. Van Harlingen, P. K. Mohseni, K. Jung and X. Li, "Anomalous Modulation of a Zero-Bias Peak in a Hybrid Nanowire-Superconductor Device", *Phys. Rev. Lett.*, **110**, 126406 (2013).

[43] A. Das, Y. Ronen, Y. Most, Y. Oreg, M. Heiblum and H. Shtrikman, "Zero-bias peaks and splitting in an Al-InAs nanowire topological superconductor as a signature of Majorana fermions", *Nature Physics*, **8**, 887-895 (2012).

[44] H. O. H. Churchill, V. Fatemi, K. Grove-Rasmussen, M. T. Deng, P. Caroff, H. Q. Xu and C. M. Marcus, "Superconductor-nanowire devices from tunneling to the multichannel regime: Zero-bias oscillations and magnetoconductance crossover", *Phys. Rev. B* **87**, 241401(R) (2013).

[45] M. T. Deng, C. L. Yu, G. Y. Huang, M. Larsson, P. Caroff and H. Q. Xu, "Parity independence of the zero-bias conductance peak in a nanowire based topological superconductor-quantum dot hybrid device", *Sci. Rep.* **4**, 7261 (2014).

[46] D. Aasen, M. Hell, R. V. Mishmash, A. Higginbotham, J. Danon, M. Leijnse, T. S. Jespersen, J. A. Folk, C. M. Marcus, K. Flensberg and J. Alicea, "Milestones Toward Majorana-Based Quantum Computing", *Phys. Rev. X*, **6**, 031016 (2016).

[47] P. Krogstrup, N. L. B. Ziino, W. Chang, S. M. Albrecht, M. H. Madsen, E. Johnson, J. Nygård, C. M. Marcus and T. S. Jespersen, "Epitaxy of semiconductor-superconductor nanowires", *Nature Materials*, **14**, 400-406 (2015).

[48] W. Chang, S. M. Albrecht, T. S. Jespersen, F. Kuemmeth, P. Krogstrup, J. Nygård and C. M. Marcus, "Hard gap in epitaxial semiconductor-superconductor nanowires", *Nature Nanotechnology*, **10**, 232-236 (2015).

[49] S. M. Albrecht, A. P. Higginbotham, M. Madsen, F. Kuemmeth, T. S. Jespersen, J. Nygård, P. Krogstrup and C. M. Marcus, "Exponential protection of zero modes in Majorana islands", *Nature*, **531**, 206-209 (2016).

[50] D. Sherman, J. S. Yodh, S. M. Albrecht, J. Nygård, P. Krogstrup and C. M. Marcus, "Hybrid Double Quantum Dots: Normal, Superconducting, and Topological Regimes", *arXiv:1605.01865* (2016).

[51] M. Stepanova and S. Dew, "Nanofabrication", *Springer-Verlag/Wien* (2012).

[52] F. Pobell, "Matter and Methods at Low Temperatures", *Berlin, Heidelberg: Springer*, 3rd ed. (2007).

[53] K. Uhlig, "Dry dilution refrigerator with ^4He-1 K-loop", *arXiv:1412.3597* (2014).

[54] Oxford Instruments plc, "Triton 200/400. Cryofree dilution refrigerator" (2012).

[55] P. N. Chubov, V. V. Eremenko, Y. A. Pilipenko, "Dependence of the Critical Temperature and Energy Gap on the Thickness of Superconducting Aluminum Films", *Sov. Phys. JETP*, **28**, 389-395 (1969).

[56] N. A. Court, A. J. Ferguson1 and R. G. Clark, "Energy gap measurement of nanostructured aluminium thin films for single Cooper-pairdevices", *Supercond Sci Technol.*, **21** (2007).

[57] I. van Weperen, S. R. Plissard, E. P. A. M. Bakkers, S. M. Frolov and L. P. Kouwenhoven, "Quantized Conductance in an InSb Nanowire", *Nano Lett.*, **13**, 387-391 (2013).

[58] H. Zhang, Önder Gül, S. Conesa-Boj, K. Zuo, V. Mourik, F. K. de Vries, J. van Veen, D. J. van Woerkom, M. P. Nowak, M. Wimmer, D. Car, S. Plissard, E. P. A. M. Bakkers, M. Quintero-Pérez, S. Goswami, K. Watanabe, T. Taniguchi and L. P. Kouwenhoven, "Ballistic Majorana nanowire devices", *arXiv:1603.04069* (2016).

[59] W. Meissner and R. Ochsenfeld, "Ein neuer effekt bei eintritt der supraleitfähigkeit", *Naturwissenschaften*, **21**, 787 (1933).

[60] F. W. London, "Macroscopic Theory of Superconductivity", *Superfluids*, (1950).

[61] D. Rainis, L. Trifunovic, J. Klinovaja and D. Loss, "Towards a realistic transport modeling in a superconducting nanowire with Majorana fermions", *Phys. Rev. B*, **87**, 024515 (2013).

[62] D. Chevallier, P. Simon and C. Bena, "From Andreev bound states to Majorana fermions in topological wires on superconducting substrates: A story of mutation", *Phys. Rev. B*, **88**, 165401 (2013).

[63] R. V. Mishmash, D. Aasen, A. P. Higginbotham and J. Alicea, "Approaching a topological phase transition in Majorana nanowires", *Phys. Rev. B*, **93**, 245404 (2016).

[64] T. D. Stanescu, R. M. Lutchyn and S. Das Sarma, "Dimensional crossover in spin-orbit-coupled semiconductor nanowires with induced superconducting pairing", *Phys. Rev. B*, **87**, 094518 (2013).

[65] C. Fasth, A. Fuhrer, L. Samuelson, V. N. Golovach and D. Loss, "Direct Measurement of the Spin-Orbit Interaction in a Two-Electron InAs Nanowire Quantum Dot", *Phys. Rev. Lett.*, **98**, 266801 (2007).

[66] E. J. H. Lee, X. Jiang, M. Houzet, R. Aguado, C. M. Lieber and S. De Franceschi, "Spin-resolved Andreev levels and parity crossings in hybrid superconductor-semiconductor nanostructures" *Nature Nanotechnology*, **9**, 79-84 (2014).

[67] W. Chang, "Superconducting Proximity Effect in InAs Nanowires", *PhD Thesis* (2014).

[68] M. Kjaergaard, "Proximity Induced Superconducting Properties in One and Two Dimensional Semiconductors", *PhD Thesis* (2015).

[69] Konrad Wölms, "Aspects of Majorana Bound States in One-Dimensional Systems with and without Time-Reversal Symmetry", *PhD Thesis* (2015).

[70] Nino Ziino, "Device Fabrication and Low Temperature Measurements of InAs Nanowires with Superconducting Al Shells", *Master Thesis* (2015).